

3D TEM Tomography of Templated Bilayer Films of Block Copolymers

Kevin W. Gotrik¹, Thomas Lam^{†2}, Adam F. Hannon¹, Wubin Bai¹, A. Alexander-Katz¹, J. Alexander Liddle², C. A. Ross^{1*}

¹ *Department of Materials Science and Engineering, Massachusetts Institute of Technology,
77 Massachusetts Avenue, Cambridge, Massachusetts 02139*

² *Center for Nanoscale Science and Technology, National Institute of Standards and Technology*

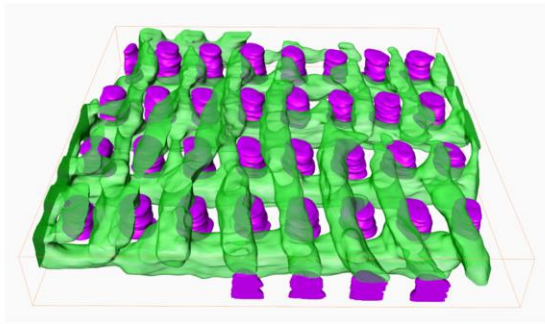
[†]*Authors contributed equally to this work*

**Address correspondence to caross@mit.edu.*

Abstract

Transmission electron microscope (TEM) tomography was used to visualize the morphology and 3D connectivity of a lithographically-templated, self-assembled bilayer film of cylinder-forming 45.5 kg/mol polystyrene-*block*-polydimethylsiloxane. The structure, formed after a 5 min solvothermal anneal, was imaged with a resolution of ≈ 3 nm in 3D, enabling a comparison between measurement and self-consistent mean-field theory (SCFT) calculations. In addition to the general agreement between modeled and measured dimensions, the tomography revealed connections between the orthogonal layers of cylinders at their crossing point, a key model prediction. Validation of the SCFT model, even under solvothermal annealing conditions, suggests that it can be used to predict the detailed nanoscale structure of features created by directed self-assembly (DSA) with confidence, which is essential in developing nanomanufacturing processes based on DSA.

Keyword: polystyrene-polydimethylsiloxane, 3D TEM Tomography, 3D Self-Assembly, Block Copolymer, Directed Self Assembly, Self-Consistent Field Theory, Model Validation



300 nm

Experimental TEM Tomography



SCFT

TOC Graphic

Current photolithographic tools, operating at a wavelength of 193 nm, are limited in their ability to produce small (< 30 nm) features at dense pitches.¹ This has led in recent years, to the adoption of a variety of double, triple, or even quadruple patterning approaches that have resulted in an erosion of the traditional cost-effectiveness of photolithography. Block copolymer (BCP) directed self-assembly (DSA) employs relatively sparse chemical or topographical lithographic features to template the periodic microdomain features of the BCP, enabling the patterning of high-resolution features and maintaining the requisite pattern-placement accuracy for advanced integrated circuit manufacture.²⁻⁷ BCPs enjoy a flexibility in chemistry so that they can be tuned for many applications, such as hard masks for bit patterned media,⁸ filtration membranes,^{9,10} electrolytes with high Li-ion conductivity,^{11,12} and nanowire¹³ or nanoparticle¹⁴ growth templates.

In order for BCP DSA to be used successfully in integrated circuit manufacturing, it is essential that validated models and design tools are available that can be used to predict the BCP features that will be generated from a given template.¹⁵ Self-consistent field theory (SCFT) has been used extensively to model the behavior of BCPs, and has been compared with transmission electron microscopy (TEM) or scanning electron microscopy (SEM) images for thin films and for BCPs confined in cylindrical or spherical pores.¹⁶ 3D TEM tomography has been applied to image microdomains in a range of bulk BCPs¹⁷⁻¹⁹ and even to study [the effects of confinement, solvent evaporation rate and nanoparticle incorporation](#).²⁰⁻²⁵ However, real-space measurements of BCP morphologies [formed by directed-self-assembly, where the templating structures and substrate are still intact, and the images are](#) of sufficient quality to enable model validation, [have](#) not previously been carried out. Soft x-ray scattering experiments and grazing incidence x-ray scattering (GISAXS) have recently enabled some direct quantitative structure comparison in thin film lamellae systems with simulations, but these methods are still indirect and require the scattering data to be converted to the real space structure profiles through computational methods.^{26,27} [In addition, such scattering methods generate ensemble measurement data and are therefore insensitive to the presence of small defect populations. In integrated circuit fabrication in particular, understanding the form and origin of such defects is essential.](#)²⁸

Here we use TEM tomography to generate high-resolution, three-dimensional reconstructions of a solvent-annealed BCP that has undergone directed self-assembly on a template consisting of posts,²⁹ and compare the results with SCFT²⁹⁻³³ calculations of the 3D microdomain structure as well as with the microdomain structure revealed by etching away the majority block. A polystyrene-*block*-polydimethylsiloxane (PS-*b*-PDMS) diblock copolymer was selected for this study because the Si content of the PDMS provides sufficient mass and phase contrast to enable the phases to be distinguished under conventional bright-field imaging conditions, without staining or etching. The contrast can be further enhanced by defocusing to a degree at which image processing techniques can be used to automatically

identify the boundaries of the two microdomains. Although the defocus degrades the resolution, at [an accelerating voltage of 200 kV, and](#) with typical defocus values of up to 3.5 μm (necessary to yield adequate contrast), a resolution of [at least](#) 3 nm can still be achieved.³⁴ This is comparable to the resolution of SCFT models, which use a coarse-graining length scale of 2.6 nm (see Supplementary Information (SI)).

Previous TEM tomography studies^{17,18} examined the morphology of bulk block copolymer systems [using samples prepared by ultramicrotomy or direct casting of thin films. Ideally, samples for TEM tomography would be in the form of cylinders to enable tilting through an angular range of \$\pm 90^\circ\$. However, in the case of a 40 nm thick BCP film on a lithographically patterned substrate, this is not possible, and the tilting range is reduced, leading to the formation of so-called “missing wedge” artifacts.](#)³⁵ ~~introduces elongation errors in the z direction. The sample preparation procedure for rod-like samples starts from $5\ \mu\text{m} \times 5\ \mu\text{m} \times 5\ \mu\text{m}$ block that is cylindrically milled to 300 nm diameter for the base with a 150 nm diameter for tip.¹¹ However, these techniques cannot be used to make electron-transparent samples from an approximately 40 nm thick BCP film on a lithographically patterned template.~~ In this study, we therefore directly fabricated samples on an electron transparent Si_3N_4 support film designed for TEM tomography. [Accounting for elongation errors,](#) we show that there is good agreement between the 3D tomographic measurements and the SCFT model, serving to validate the model and to reveal details of the morphology of the [two ordered layers of orthogonal cylinders](#): in particular the existence of connections between cylinders at the crosspoints. Furthermore, we used reactive ion etching (RIE) to treat the sample and compare pre- and post-processed tomographic data with data obtained by conventional SEM. We were not only able to assess the degree to which RIE changes the structure of the PDMS microdomains, but were also able to determine whether conventional, two-dimensional imaging provides a useful representation of these complex, three-dimensional structures.

The SCFT method is described in the SI and in previous studies.²⁹ The system was modeled using periodic boundary conditions with dimensions and geometry that reflect those encountered in the experiment. To account for the solvent annealing process, the film was treated as being swelled by solvent, with an effective volume fraction of PDMS, and a Flory-Huggins interaction parameter dependent upon the ratio of solvents used in the annealing. Additionally, this polymer has a high χ parameter (usually cited as 0.26^{36,37} but recently calculated to be ≈ 0.14 at room temperature³⁸). This means that during the solvent annealing process used here, the BCP is still below its order-disorder transition temperature and equilibrium microphase separation therefore occurs during the solvent annealing itself rather than during the quench from a disordered state.²⁷ It is therefore reasonable to carry out SCFT simulations of microphase separation by using an effective χ to include the solvent, rather than

by modeling the solvent explicitly.³⁹ Unlike our prior work which included a range of post periods,²⁹ here we focus on a single post period but vary post height, effective χ , and effective volume fraction.

Fig. 1 is a flow diagram showing the process for preparing samples. Details of the methods, as well as the TEM tomography procedure, are given in the Methods section. The template was prepared by electron beam lithography and development of hydrogen silsesquioxane (HSQ) resist, spin-coated on a nitride membrane, to form an array of HSQ posts. This was spin-coated with PS-*b*-PDMS to a thickness of 32 nm, then followed by a solvothermal anneal to induce microphase separation.

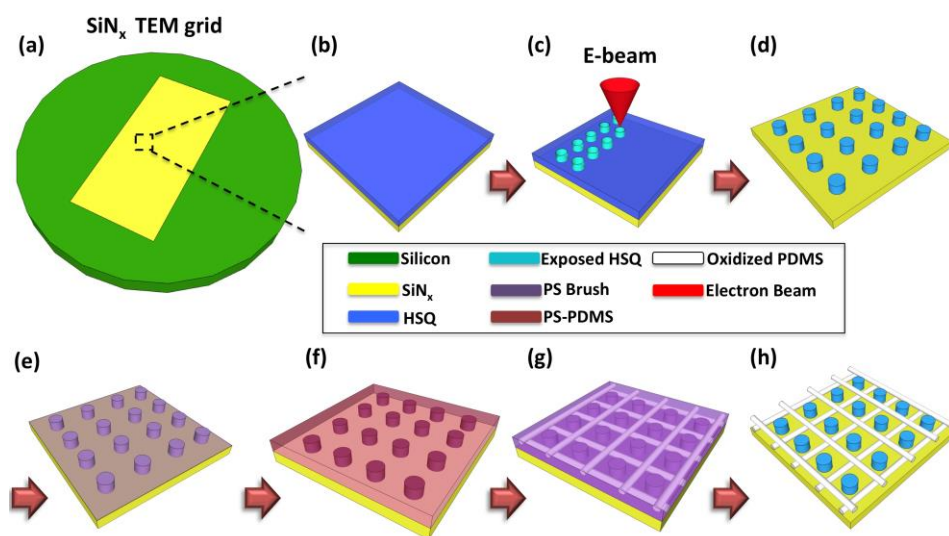


Figure 1. Schematic of the sample fabrication. (a) SiN_x TEM grid, (b) spin coat HSQ resist, (c) electron beam lithography to expose the array of posts, (d) salty development of HSQ, (e) polystyrene brush treatment of posts and substrate, (f) spin coat PS-*b*-PDMS block copolymer, (g) solvothermal annealing

to produce in-plane cylindrical PDMS microdomains in a PS matrix, (h) reactive ion etching to remove the PDMS surface layer then the PS matrix. TEM tomography is carried out at steps (g) and (h).

Fig. 2 shows (a,b) TEM and (c,d) SEM micrographs of the self-assembled microdomains before (a) and after (b-d) reactive ion etching to remove the PS matrix and oxidize the PDMS microdomains. In Fig. 2(a), an image of the unetched templated film, the darkest circular features are the HSQ posts, seen from the top. Between each row of posts is a dark line indicating the presence of a PDMS cylinder. The cylinders running left to right are most clearly seen, but an orthogonal set running from top to bottom is also visible. Fig. 2(b) shows a different region of the sample after oxygen RIE, which removed the PS, enhancing the contrast of the cylinders. The majority of the image showed orthogonal cylinders, but in some regions cylinder curvature and junctions are visible. 3D reconstructions and visualizations were performed in the dashed inset regions in Fig. 2 (a,b). In the SI, the video S1 is of the reconstructed image stack (before the image stack was aligned for quantification) moving from top surface into the substrate plane of the unetched film. Fig. 2(c) and (d) show top view and tilted SEM images respectively of an etched sample prepared in a similar manner to give a sense of the topography of the oxidized PDMS after etching. From the etched sample it is difficult to determine the relationship between the top and bottom cylinders before etching, for example to determine the presence or absence of junctions between cylinders.

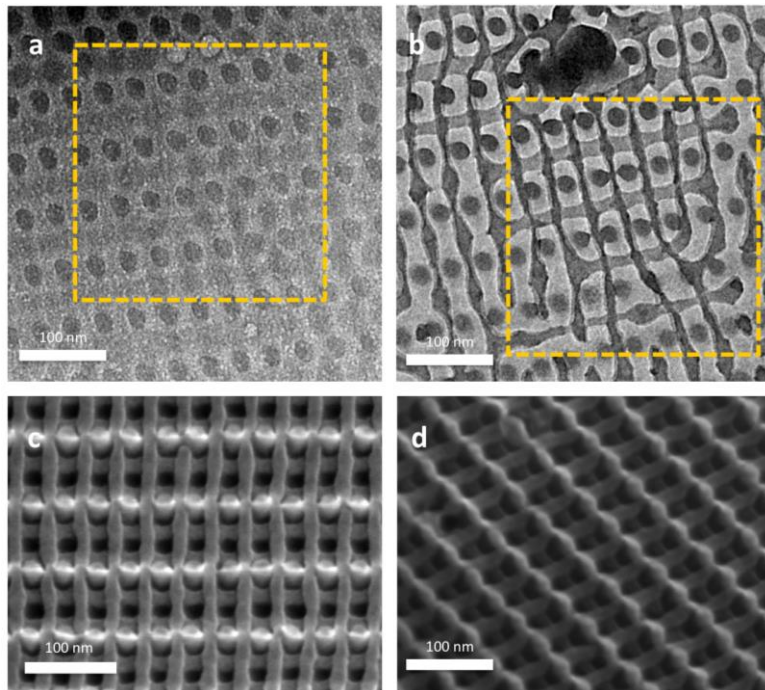


Figure 2. TEM of (a) unetched sample and (b) after oxygen etch. (c) Top view and (d) tilted view SEM images of another sample after RIE, made on an oxidized Si substrate using a similar process but with pillar spacing $d_x=36$ nm, $d_y=62$ nm, after RIE.

Fig. 3 shows the 3D visualization of the unetched sample (Fig. 3(a)) and for comparison a visualization of the etched sample (Fig. 3(b)). Fig. 3a has been labeled so that posts and cylinders can be identified. Videos S2 and S3 in the SI are 3D tomography videos of unetched and etched structures respectively. From the TEM tomography a pillar spacing of $d_x=34$ nm, $d_y=65$ nm was measured in the unetched sample. It is clear that over the majority of the sample, the mesh of orthogonal cylinders formed interconnections at the crossing points. In the bottom left corner a third layer of cylinders started to form, and the cylinders between rows of posts X4 and X6 had discontinuous diameters.

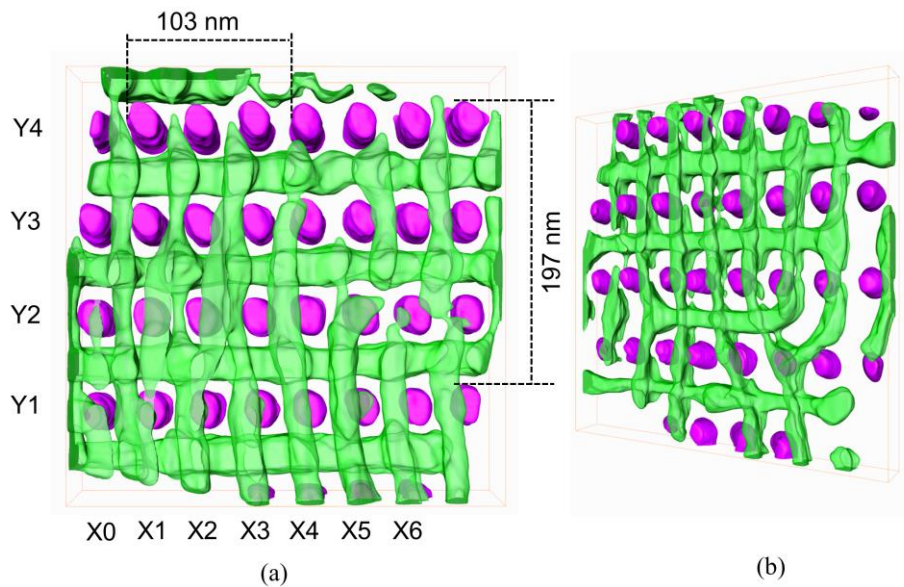


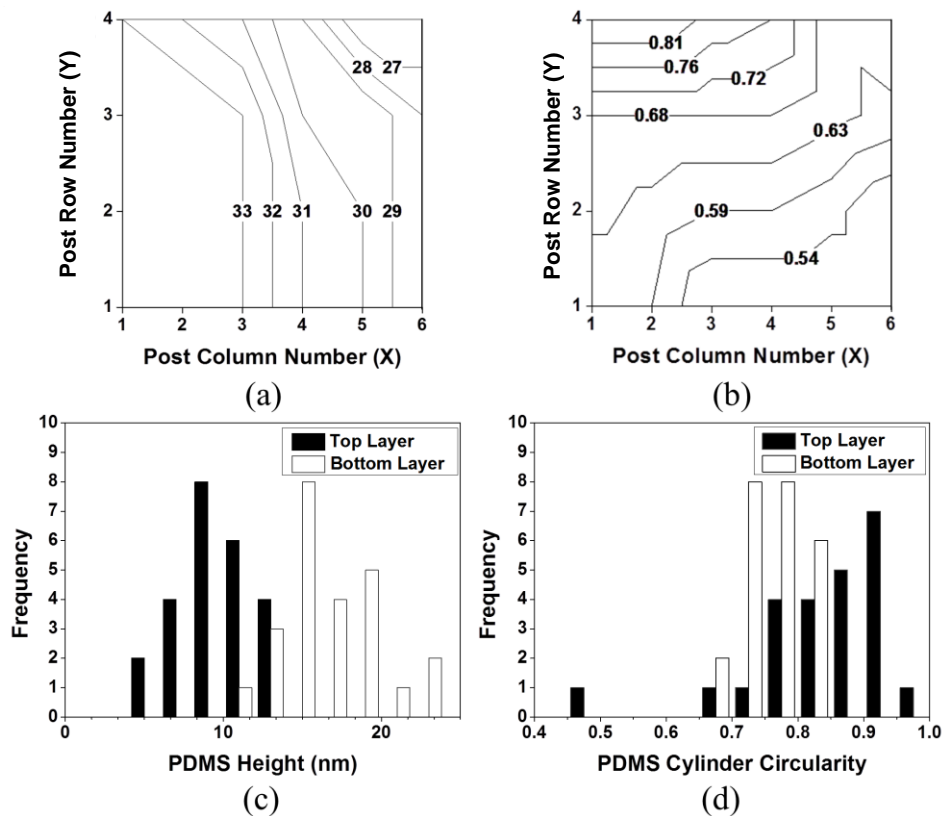
Figure 3 a) 3D visualization of the unetched structure and annotation of columns of HSQ posts marked X, and rows of HSQ posts marked Y with a bounding box volume of $296 \text{ nm} \times 296 \text{ nm} \times 42 \text{ nm}$. (Top-down view) b) After etching, PDMS cylinders are presented in lighter transparent green and HSQ in purple with a bounding box volume of $296 \text{ nm} \times 296 \text{ nm} \times 31 \text{ nm}$.

From the analysis of the 3D visualized features of the unetched sample, quantitative statistics are presented in **Fig. 4**. Within this region of the film a thickness gradient is present shown by the contour plot in Fig. 4(a), such that the left hand side had a thickness $> 33 \text{ nm}$ and the right hand side was $< 30 \text{ nm}$. A gradient is also present in HSQ post height h_p , shown in the contour plot in Fig. 4(b). So that the results can be compared with SCFT modeling, the HSQ post heights were expressed as h_p/L_0 , where L_0 is the equilibrium cylinder period for the film on a smooth substrate, approximately 36 nm . The average diameter of the HSQ posts was $(20 \pm 1) \text{ nm}$ with a measured circularity of 0.86 ± 0.01 , the tabulated statistics of which found in Table SI in the SI. Circularity is defined as $4\pi[\text{area}]/[\text{perimeter}]^2 = 1$ for a circle and < 1 for an ellipse. Unless noted otherwise all measurement uncertainties are quoted as (average \pm one standard deviation).

Commented [LJA1]: Do these numbers need to be adjusted to take account of the elongation factor?

Commented [LJA2]: Ditto

Tomography revealed differences between the top and bottom layers of PDMS cylinders. PDMS cylinders in the bottom layer were thicker in the direction perpendicular to the substrate plane, with a peak in the distribution of cylinder diameters at 14 nm, in comparison to the top layer of cylinders with peak at 8 nm, Fig. 4(c). The bottom-layer PDMS cylinders were also more elliptical in cross-section with many measurements of circularity between 0.75 and 0.85 and the major axis parallel to the film plane, whereas the top layer cylinders had circularity > 0.85 (Fig. 4(d)). Tables SII-SIV of the tabulated statistics to generate Fig. 4 (b-d) can be found in the SI.



Commented [LJA3]: Dose the circularity data need to be updated?

Figure 4. Quantitative measurements from TEM tomography. (a) Contour plot of the total thickness of the PS-*b*-PDMS film, the contour lines are in units of nm. The axes represent the position within the sample area indexed with respect to the rows and columns of posts, the contour lines are in units of nm.

(b) HSQ post heights plotted as h_p/L_0 at different positions within the sample area. (c) Histogram of PDMS cylinder heights measured in the out of plane direction for top and bottom layers. (d) Histogram of PDMS circularity for top and bottom layers.

We now compare these findings to the results of the SCFT modeling. **Fig. 5** summarizes the morphologies predicted from SCFT for two different volume fractions $f = 0.32$ and 0.36 , three values of $\chi N = 18, 24$ and 30 and three different substrate functionalizations: top (air) surface and bottom (substrate) surface neutral to the two blocks; top surface preferential to PDMS and bottom surface neutral; and top surface preferential to PDMS and bottom surface preferential to PS. The posts themselves were always preferential to PS in the model. These values of χN and f were chosen to be relevant to solvent annealing, which reduces χ as solvent is incorporated, and changes the effective f of the minority component if the solvent is selective.²⁷ The range of χN values chosen for the simulations are below those predicted for the neat block copolymer (lower limit of $\chi N = 68$ based on $\chi = 0.14$ ³⁸ and upper limit of $\chi N = 126$ based on $\chi = 0.26$ ^{37,40} with $N = 486$ for 45.5 kg/mol PS-*b*-PDMS) due to both the coarse-graining of the model which includes only 125 segments per chain and the incorporation of solvent which lowers χ by an amount proportional to the fraction of polymer volume. The exact correspondence with the effective χN is not known *a priori* so multiple values were chosen and the best match with experimental results used for comparison. For each of these combinations, simulations were done over a range of post heights h_p . Fifteen distinct microdomain morphologies were identified and are labeled and color coded in Fig. 5(a-l). The upper panels of Fig. 5 show which morphology was found for each combination of $\chi N, f$, surface affinity and h_p . Of interest, the dark blue represents cross-point structures where the upper and lower cylinders are connected at a junction. The results of the simulations suggests that $\chi N = 18$ is a lower bound to the formation of the cross-point structure as the structure was only observed for higher values of χN .

Based on the application of a PS brush to the substrate, and the lower surface energy of PDMS compared to PS, we would expect the simulation with top surface preferential to PDMS and bottom surface preferential to PS to best represent the experiment. However, the TEM data suggests that the bottom layer of cylinders contacted the substrate, though it was difficult to detect contrast between the PS and the amorphous nitride layer. Contact between PDMS and the substrate would indicate that the substrate did not have a strong affinity for PS, i.e. the actual substrate surface energy conditions were somewhere between neutral and fully preferential to the PS, possibly due to poor grafting of the PS brush

on the nitride substrate. (The brush grafts well to the HSQ posts making them attractive to the PS.) Additionally, a PDMS surface layer was not observed in the TEM data, suggesting that the solvent vapor reduced the preference for PDMS to wet the surface. Further evidence of this was found in RIE experiments on samples annealed in different solvent ratios (see SI), in which the PDMS surface layer is suppressed as the toluene:heptane ratio increased. These observations motivated the modeling of a neutral top and bottom surface.

In the simulations with neutral top and bottom surfaces (and PS-preferential posts), an equilibrium film thickness of $2.0 L_0$ was required to produce two layers of cylinders, unlike the $3.0 L_0$ thickness for a PS-preferential bottom surface and PDMS top surface where surface layers are present. The neutral surface conditions yielded interconnected cylinders over a range of post heights from $0.71 L_0$ to $1.43 L_0$ and for $\chi N = 24$ and 30 for both volume fractions. For $f = 0.32$ and $\chi N = 30$ there was also a small post height range of $1.21 L_0$ - $1.29 L_0$ (dark green) where a mesh structure without interconnections was observed, but this post height exceeded the actual post height in the experiment, which was closer to $0.9 L_0$. Making the top surface preferential to PDMS and the bottom surface to PS restricted the range of post heights in which interconnected cylinders formed. The simulations scanned a larger range of post heights than experiment to ensure determine whether there was a minimum height where the mesh structure formed in addition to simply exploring the morphologies formed at the other post height conditions

From the height of each post h_p and the film thickness determined from tomography data, the expected morphology around each post can be calculated, and is given in Table SII in the SI. SCFT predicts that the top left region of the film (HSQ posts A-D) would form a connected mesh structure whereas the remainder of the sample made up of shorter posts would form disconnected cylinders, based on neutral surface wetting conditions and $\chi N = 24$ or 30 . Experimentally, interconnections were seen throughout the sample, indicating that interconnections formed at lower post heights than predicted by the model.

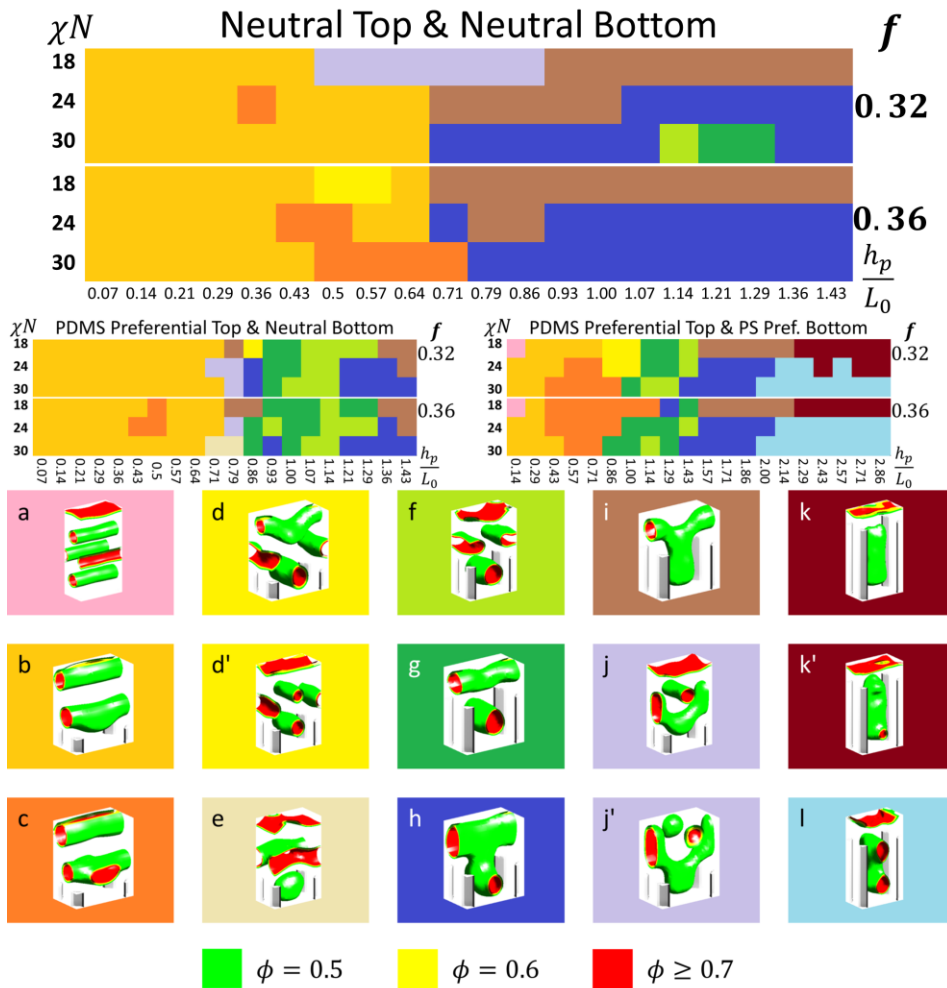
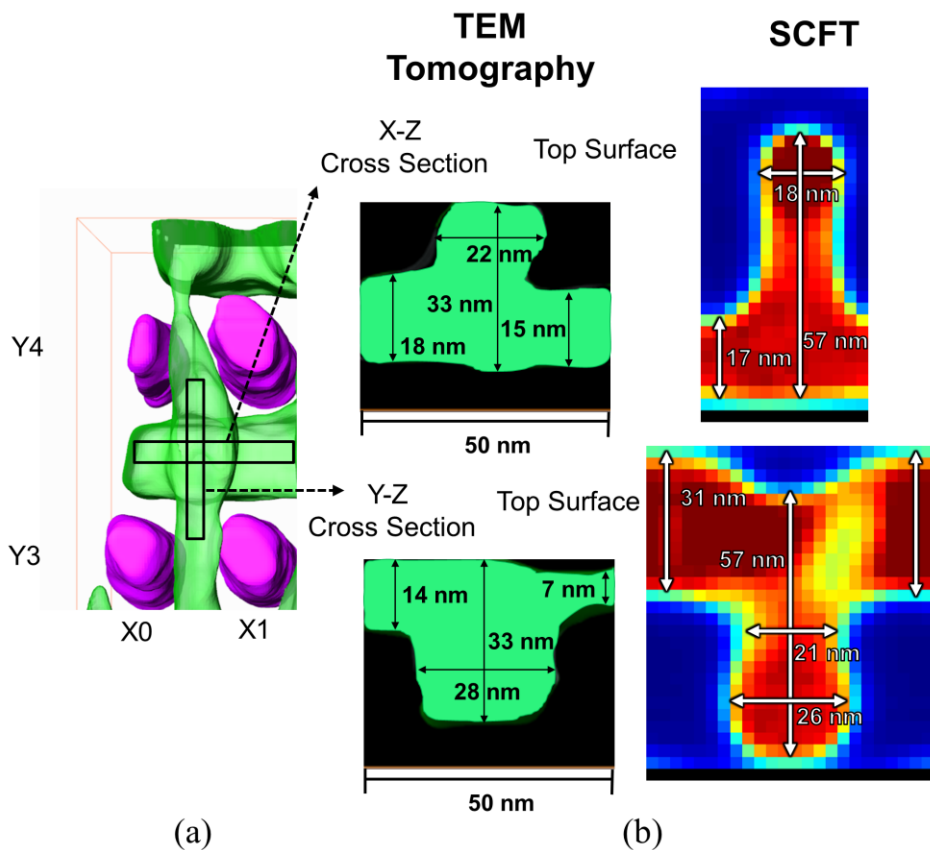


Figure 5. Top: Phase diagrams showing the morphologies predicted under different simulation conditions. The colors correspond to the morphologies shown in (a-l), with dark blue representing the connected mesh structure. The phase diagrams were calculated as a function of normalized post height $\frac{h_p}{L_0}$ for $f = 0.32$ and 0.36 , $\chi N = 18, 24$ and 30 , and three different surface wetting conditions. Bottom: morphologies were (a) triple layers of cylinders, (b) double layers of cylinders/lamellae, (c) cylinder over perforated lamellae, (d) mesh single cylinder over double layer of cylinders or (d') triple layer of cylinders, (e) cylinder over sphere, (f) double layer parallel cylinders, (g) mesh structure (no connection),

(h) mesh structure (connected), (i) cylinder with perpendicular cylinder, (j) flipped mesh structure (not connected) or (j') sphere over curved cylindrical structure, (k) perpendicular cylinder or (k') perpendicular cylinder with bottom connection, and (l) double connected structure.

Fig. 6 shows a detailed comparison of TEM tomography and SCFT at the cross sections of a connected mesh structure. In Fig. 6a the top region (Y4 and X1 quadrant) is highlighted, where the SCFT calculations predicted the formation of connected mesh structures. Cross-sections in the X - Z and Y - Z planes are shown. The SCFT was calculated for a film thickness of 57 nm (Fig. 6b), which corresponds to the observed thickness of 33 nm for the dry film multiplied by a swelling ratio near 2. The model is limited to finding equilibrium structures in the swollen film state, so all correspondence between experimental results and SCFT results need to consider an effective collapse factor of ≈ 0.5 between the results. Future work with alternative dynamical models that are being developed can try to close this gap between simulations and experiments.³⁹ Upon quenching, the structure is assumed to collapse in the Z -direction as solvent is removed, reducing the out-of-plane dimensions of the microdomains and leading to elliptical cross-section cylinders as seen experimentally. The PDMS dimensions and shape in both X and Y -directions from SCFT match well to the TEM cross section measurements when the deswelling is considered, and the reduced circularity of the bottom layer PDMS is explained by the film collapsing during quenching. The measurement differences are all within the error range of measured periodicity changes of recent *in situ* GISAXS measurements.²⁷



Commented [LJA4]: Do these visualizations need to be scale?

Figure 6. (a) Location of the X-Z and X-Y cross section. (b) TEM tomography and SCFT comparison for the connected mesh structure.

We finally discuss the effect of O₂ RIE on the structure. Fig. 3b shows the oxidized PDMS cylinders and the posts after removing the PS with oxygen. The etching produced a further shrinkage of the PDMS features in the Z-direction, as well as some reduction in the in-plane PDMS dimensions (but not the period), particularly affecting the upper layer of cylinders. Additionally, the HSQ cylindrical posts became conical upon etching. This shows that etching preserved the overall pattern geometry in the structure, although it led to a shrinkage in the PDMS features. With these considerations, the structure of the film after drying can be deduced from its appearance after etching.

In conclusion, 3D TEM tomography allowed for characterization of the 3D structure of a solvent annealed, templated block copolymer film without staining or etching, by the expedient of preparing samples on TEM grids. A direct image of the 3D templated structure without the distortions caused by etching provides valuable insight into microdomain morphology resulting from solvent anneal, and helps to inform SCFT simulations, validating their application for solvent annealed samples in the strong segregation limit where the polymer is modeled in its swelled state with effective χ and f resulting from solvent incorporation. The results demonstrated interconnections in a crossbar structure templated by posts, as predicted by the SCFT simulations for a range of post heights, χN , f and surface chemistry. The results also gave indications of the surface affinity of the substrate and the air interface, based on the presence or absence of wetting layers. Etching reduced the in-plane dimensions of the PDMS cylinders, particularly those in the upper layer, and tapered the posts into truncated conical shapes. These methods can be applied to similar structures in the future to allow both characterization and design of templates for directed self-assembly.

Methods

Template fabrication. A scanning electron beam system was used to fabricate the post array of negative tone HSQ resist (Dow Corning XR-1541 2% solids). (40 ± 2) nm HSQ was spun cast (3000 RPM) on a 3 mm diameter Si_3N_4 TEM grid (two nitride windows of $0.1 \text{ mm} \times 1.5 \text{ mm}$) which consisted of a 50 nm thick prime Si_3N_4 support film acting as the window. A 125-kV acceleration voltage, 1 nA electron beam was used to expose the HSQ resist in the center region of the windows. This exposure was done by point exposure with a dwell time at each coordinate of 70 μs to 100 μs . Shortly after exposure, a 4% NaCl/1% NaOH by mass DI water salty-developer solution was used to develop the exposed samples for 4 min at room temperature with moderate agitation. The sample was then exposed to 2 min of DI water to remove residual developer solution and then 10 s in IPA to reduce surface capillary forces that could strain or break patterned features or the TEM grid window itself before the film was dried using N_2 gas. Finally, an oxygen plasma asher (50 W, 46 Pa (0.35 Torr)) was used to clean residual HSQ from the surface and harden the HSQ pattern for 2 min yielding the post pattern with post heights of (38 ± 2) nm.

Block copolymer self-assembly. The Si_3N_4 substrates with HSQ posts were chemically functionalized with hydroxyl-terminated PS (11 kg mol^{-1} , PolymerSource) by spinning solutions of the brush then baking the samples in a vacuum oven for 16 hr at a pressure of $\approx 2600 \text{ Pa}$ ($\approx 20 \text{ Torr}$) and temperature of 170°C . After baking, the samples were rinsed with toluene to remove unreacted brush and then dried

using N₂ gas. 45.5 kg/mol PS-*b*-PDMS (Polymer Source, Inc. P7517-SDMS, $f_{\text{PDMS}} = 0.32$) as 2 wt.% in PGMEA solution at 272 rad·s⁻¹ (2650 RPM) was spun cast onto the brush-treated TEM grid.

Solvent annealing. Solvothermal vapor annealing was performed on the samples using methods that produced a crossbar-like structure of PDMS cylinders from 45.5 kg/mol PS-*b*-PDMS. This is explained in previous work describing a rapid annealing system.⁴¹ Briefly, a 5:1 by volume saturated vapor of toluene:n-heptane was prepared in an annealing chamber. Then, the TEM grid was rapidly (to prevent solvent vapor loss) placed in the environment on top of an ambient temperature resistive heater. After 4.5 min, the resistive heater was turned on and allowed to heat for 30 s from room temperature (23 ± 1) °C to (43 ± 1) °C. The heating drives out the solvent from the film and ends the annealing. Afterwards, the TEM grid is removed from the annealing chamber.

Following the solvent annealing, the TEM grid was imaged directly by TEM tomography or subjected to reactive ion etching, where a 5 s CF₄ reactive ion etch (RIE) with power 50 W and pressure 2 Pa (15 mTorr) was performed to remove any PDMS surface layer. A 22 s oxygen RIE with power 90 W and pressure 0.8 Pa (6 mTorr) immediately followed in order to oxidize the underlying PDMS cylinders and remove the surrounding PS matrix. SEM images were then obtained.

TEM tomography. TEM tomography was performed on both pre- and post- reactive ion-etched, solvothermal-annealed BCP films prepared on an electron transparent Si₃N₄ support film. Using a TEM tomography holder and an operating voltage of 200kV, bright-field images were collected at a constant defocus value through a tilt range of negative 60° to positive 60° (at 5° increments from negative 45° to positive 45° and in 3° increments from 45° to 60°). The tilt increments were chosen to optimize the tradeoff between image resolution and beam damage. The elongation error predicted by the model of Kawase *et al.* that results from constraining the tilt angles between ± 60° is ≈ 1.16 in the z-direction.³⁵ Images were recorded with 4x pixel binning, giving a 512 × 512 pixel array, using a charge-coupled detector (CCD). Tilt series images were corrected for spatial misalignment using cross correlation, and the tilt axis was identified using semi-automated methods in a commercial tomography reconstruction software package. Reconstruction was performed using the simultaneous iterative reconstruction technique (SIRT) algorithm applied through the same software. A volume of 296 nm × 296 nm × 42 nm with a voxel size of 1 nm × 1 nm × 1 nm was reconstructed for the unetched film. As noted above, due to the discrete sampling of Fourier space and missing wedge artifacts the resolution parallel to the optic axis (z-depth) is expected to be different from the in-plane resolution in the reconstructed volume. The resolution, δ , in z can be estimated from the sample thickness and maximum tilt angle as $\delta \approx t/100 \times \cos\theta_{\text{max}}$. For a thickness of 92 nm (where the transparent Si₃N₄ support and the

unetched BCP films are 50 and 42 nm, respectively) the resolution in z is ≈ 2 nm.⁴² Segmentation (thresholding) was performed manually on the reconstructed image stack to define the features to produce the surface rendering of the reconstruction through commercial tomography visualization software. Segmentation by this method introduces an uncertainty of < 2 nm. The resulting segmented image stacks were rotated to align the cross bar structures with the x and y axes of the reconstruction and remove a slight incline of the film. A 3 pixel (approximately 3 nm) median filter was also applied to the visualized features (surface rendering) of the image stack as a smoothing operation, consistent with the theoretical resolution limit of TEM tomography performed under these conditions. The rendered features were then measured to determine the average diameters, circularity, and heights of the template HSQ posts using slice-by-slice analysis. The PDMS cylinder average diameters and circularity were measured in the same way in the regions where the cylinders were unconnected to neighboring PDMS cylinders. In regions where the PDMS cylinders were connected, only the overall thickness was measured. For visualization, but not quantitative analysis, of the reconstructed 3D volume, smoothing was applied in the visualization software.

Acknowledgement. The authors gratefully acknowledge support of the Semiconductor Research Corporation; the C-SPIN Center, a STARnet Center supported by MARCO and DARPA; Tokyo Electron; Taiwan Semiconductor Manufacturing Company; and the National Science Foundation. The authors would also like to thank Jonathan Winterstein (CNST-NIST) for helpful discussions on image resolution of defocus bright-field TEM tomography.

Supporting Information Available: Additional figures, videos, simulation information, and SEM micrographs are found in the supplementary online material which is available free of charge *via* the internet.

Disclaimer: Certain commercial equipment, instruments, or materials are identified in this report in order to specify the experimental procedure adequately. Such identification is not intended to imply recommendation or endorsement by the National Institute of Standards and Technology, nor is it intended to imply that the materials or equipment identified are necessarily the best available for the purpose.

References

- (1) Sanders, D. P. Advances in Patterning Materials for 193 Nm Immersion Lithography. *Chem. Rev.* **2010**, *110*, 321–360.
- (2) Ruiz, R.; Kang, H.; Detcherry, F. A.; Dobisz, E.; Kercher, D. S.; Albrecht, T. R.; DePablo, J. J.; Nealey, P. F. Density Multiplication and Improved Lithography by Directed Block Copolymer Assembly. *Science (80-.)*. **2008**, *321*, 936–939.
- (3) Stoykovich, M. P.; Müller, M.; Kim, S. O.; Solak, H. H.; Edwards, E. W.; de Pablo, J. J.; Nealey, P. F. Directed Assembly of Block Copolymer Blends into Nonregular Device-Oriented Structures. *Science (80-.)*. **2005**, *308*, 1442–1446.
- (4) Park, S.-M.; Liang, X.; Harteneck, B. D.; Pick, T. E.; Hiroshiba, N.; Wu, Y.; Helms, B. A.; Olynick, D. L. Sub-10 Nm Nanofabrication via Nanoimprint Directed Self-Assembly of Block Copolymers. *ACS Nano* **2011**, *5*, 8523–8531.
- (5) Darling, S. B. Directing the Self-Assembly of Block Copolymers. *Prog. Polym. Sci.* **2007**, *32*, 1152–1204.
- (6) Stoykovich, M. P.; Nealey, P. F. Block Copolymer Lithography: Periodic Arrays of 10¹¹ Holes in 1 Square Centimeter. *Science (80-.)*. **1997**, *276*, 1401–1404.
- (7) Bao, X.-Y.; Yi, H.; Bencher, C.; Chang, L.; Dai, H.; Chen, Y.; Chen, P.-T. J. J.; Wong, H.-S. P. P. SRAM, NAND, DRAM Contact Hole Patterning Using Block Copolymer Directed Self-Assembly Guided by Small Topographical Templates. (*IEDM*), *2011 IEEE* **2011**, 7.7.1 –7.7.4.
- (8) Terris, B. D.; Thomson, T. Nanofabricated and Self-Assembled Magnetic Structures as Data Storage Media. *J. Phys. D: Appl. Phys.* **2005**, *38*, R199–R222.
- (9) Yang, S. Y.; Ryu, I.; Kim, H. Y.; Kim, J. K.; Jang, S. K.; Russell, T. P. Nanoporous Membranes with Ultrahigh Selectivity and Flux for the Filtration of Viruses. *Adv. Mater.* **2006**, *18*, 709–712.
- (10) Jackson, E. A.; Hillmyer, M. A. Nanoporous Membranes Derived from Block Copolymers: From Drug Delivery to Water Filtration. *ACS Nano* **2010**, *4*, 3548–3553.
- (11) Soo, P. P.; Huang, B.; Jang, Y.-I.; Chiang, Y.-M.; Sadoway, D. R.; Mayes, A. M. Rubbery Block Copolymer Electrolytes for Solid-State Rechargeable Lithium Batteries. *J. Electrochem. Soc.* **1999**, *146*, 32–37.
- (12) Xiao, Q.; Wang, X.; Li, W.; Li, Z.; Zhang, T.; Zhang, H. Macroporous Polymer Electrolytes Based on PVDF/PEO-B-PMMA Block Copolymer Blends for Rechargeable Lithium Ion Battery. *J. Memb. Sci.* **2009**, *334*, 117–122.

- (13) Thurn-Albrecht, T.; Schotter, J.; Kästle, G. A.; Emley, N.; Shibauchi, T.; Krusin-Elbaum, L.; Guarini, K.; Black, C. T.; Tuominen, M. T.; Russell, T. P. Ultrahigh-Density Nanowire Arrays Grown in Self-Assembled Diblock Copolymer Templates. *Science* (80-.). **2000**, *290*, 2126–2129.
- (14) Haryono, A.; Binder, W. H. Controlled Arrangement of Nanoparticle Arrays in Block-Copolymer Domains. *Small* **2006**, *2*, 600–611.
- (15) Ginzburg, V. V.; Weinhold, J. D.; Trefonas, P. Computational Modeling of Block-Copolymer Directed Self-Assembly. *J. Polym. Sci. Part B Polym. Phys.* **2013**, n/a–n/a.
- (16) Wu, Y.; Cheng, G.; Katsov, K.; Sides, S. W.; Wang, J.; Tang, J.; Fredrickson, G. H.; Moskovits, M.; Stucky, G. D. Composite Mesostuctures by Nano-Confinement. *Nat. Mater.* **2004**, *3*, 816–822.
- (17) Spontak, R. J.; Williams, M. C.; Agard, D. A. Three-Dimensional Study of Cylindrical Morphology in a Styrene-Butadiene-Styrene Block Copolymer. *Polymer (Guildf)*. **1988**, *29*, 387–395.
- (18) Spontak, R. J.; Fung, J. C.; Braunfeld, M. B.; Sedat, J. W.; Agard, D. A.; Kane, L.; Smith, S. D.; Satkowski, M. M.; Ashraf, A.; Hajduk, D. A.; *et al.* Phase Behavior of Ordered Diblock Copolymer Blends: Effect of Compositional Heterogeneity. *Macromolecules* **1996**, *29*, 4494–4507.
- (19) Midgley, P. A.; Ward, E. P. W.; Hungria, A. B.; Thomas, J. M. Nanotomography in the Chemical, Biological and Materials Sciences. *Chem. Soc. Rev.* **2007**, *36*, 1477–1494.
- (20) Xu, T.; Zvelindovsky, A. V.; Sevink, G. J. A.; Lyakhova, K. S.; Jinnai, H.; Russell, T. P. Electric Field Alignment of Asymmetric Diblock Copolymer Thin Films. *Macromolecules* **2005**, *38*, 10788–10798.
- (21) Bae, D.; Jeon, G.; Jinnai, H.; Huh, J.; Kim, J. K. Arrangement of Block Copolymer Microdomains Confined inside Hemispherical Cavities. *Macromolecules* **2013**, *46*, 5301–5307.
- (22) McKenzie, B. E.; Nudelman, F.; Bomans, P. H. H.; Holder, S. J.; Sommerdijk, N. A. J. M. Temperature-Responsive Nanospheres with Bicontinuous Internal Structures from a Semicrystalline Amphiphilic Block Copolymer. *J. Am. Chem. Soc.* **2010**, *132*, 10256–10259.
- (23) Chen, C.-K.; Hsueh, H.-Y.; Chiang, Y.-W.; Ho, R.-M.; Akasaka, S.; Hasegawa, H. Single Helix to Double Gyroid in Chiral Block Copolymers. *Macromolecules* **2010**, *43*, 8637–8644.
- (24) Thorkelsson, K.; Mastroianni, A. J.; Ercius, P.; Xu, T. Direct Nanorod Assembly Using Block Copolymer-Based Supramolecules. *Nano Lett.* **2012**, *12*, 498–504.

- (25) Li, Z.; Hur, K.; Sai, H.; Higuchi, T.; Takahara, A.; Jinnai, H.; Gruner, S. M.; Wiesner, U. Linking Experiment and Theory for Three-Dimensional Networked Binary Metal Nanoparticle-Triblock Terpolymer Superstructures. *Nat. Commun.* **2014**, *5*, 3247.
- (26) Sunday, D. F.; Hammond, M. R.; Wang, C.; Wu, W.; Kline, R. J.; Stein, G. E. Three-Dimensional X-Ray Metrology for Block Copolymer Lithography Line-Space Patterns. *J. Micro/Nanolithography, MEMS, MOEMS* **2013**, *12*, 031103.
- (27) Gu, X.; Gunkel, I.; Hexemer, A.; Gu, W.; Russell, T. P. An in Situ Grazing Incidence X-Ray Scattering Study of Block Copolymer Thin Films during Solvent Vapor Annealing. *Adv. Mater.* **2014**, *26*, 273–281.
- (28) Defect reduction and defect stability in IMEC's 14nm half-pitch chemo-epitaxy DSA flow | (2014) | Gronheid | Publications | Spie
<http://spie.org/Publications/Proceedings/Paper/10.1117/12.2047265> (accessed Jul 2, 2014).
- (29) Tavakkoli K G, A.; Gotrik, K. W.; Hannon, A. F.; Alexander-Katz, A.; Ross, C. A.; Berggren, K. K. Templating Three-Dimensional Self-Assembled Structures in Bilayer Block Copolymer Films. *Science* **2012**, *336*, 1294–1298.
- (30) Fredrickson, G. H. The Equilibrium Theory of Inhomogeneous Polymers
<http://www.oxfordscholarship.com/view/10.1093/acprof:oso/9780198567295.001.0001/acprof-9780198567295>.
- (31) Fredrickson, G. H.; Ganesan, V.; Drolet, F. Field-Theoretic Computer Simulation Methods for Polymers and Complex Fluids. *Macromolecules* **2002**, *35*, 16–39.
- (32) Mickiewicz, R. A.; Yang, J. K. W.; Hannon, A. F.; Jung, Y.-S.; Alexander-Katz, A.; Berggren, K. K.; Ross, C. A. Enhancing the Potential of Block Copolymer Lithography with Polymer Self-Consistent Field Theory Simulations. *Macromolecules* **2010**, *43*, 8290–8295.
- (33) Tavakkoli K G, A.; Hannon, A. F.; Gotrik, K. W.; Alexander-Katz, A.; Ross, C. A.; Berggren, K. K. Rectangular Symmetry Morphologies in a Topographically Templated Block Copolymer. *Adv. Mater.* **2012**, *24*, 4249–4254.
- (34) Frank, J. *Electron Tomography: Methods for Three-Dimensional Visualization of Structures in the Cell*; Springer, 2008; p. 470.
- (35) Kawase, N.; Kato, M.; Nishioka, H.; Jinnai, H. Transmission Electron Microtomography without the “Missing Wedge” for Quantitative Structural Analysis. *Ultramicroscopy* **2007**, *107*, 8–15.
- (36) Nose, T. Coexistence Curves of Polystyrene/ Poly(dimethylsiloxane) Blends. *Polymer (Guildf)*. **1995**, *36*, 2243–2248.
- (37) Jung, Y. S.; Ross, C. A. Orientation-Controlled Self-Assembled Nanolithography Using a Polystyrene-Polydimethylsiloxane Block Copolymer. *Nano Lett.* **2007**, *7*, 2046–2050.

- (38) Kennemur, J. G.; Yao, L.; Bates, F. S.; Hillmyer, M. A. Sub-5 Nm Domains in Ordered Poly(cyclohexylethylene)- Block -Poly(methyl Methacrylate) Block Polymers for Lithography. *Macromolecules* **2014**, *47*, 1411–1418.
- (39) Paradiso, S. P.; Delaney, K. T.; García-Cervera, C. J.; Cenicerros, H. D.; Fredrickson, G. H. Block Copolymer Self Assembly during Rapid Solvent Evaporation: Insights into Cylinder Growth and Stability. *ACS Macro Lett.* **2014**, *3*, 16–20.
- (40) Nose, T. Coexistence Curves of Polystyrene/ Poly(dimethylsiloxane) Blends. *Polymer (Guildf)*. **1995**, *36*, 2243–2248.
- (41) Gotrik, K. W.; Ross, C. A. Solvothermal Annealing of Block Copolymer Thin Films. *Nano Lett.* **2013**, *13*, 5117–5122.
- (42) Midgley, P. A.; Dunin-Borkowski, R. E. Electron Tomography and Holography in Materials Science. *Nat. Mater.* **2009**, *8*, 271–280.

3D TEM Tomography of Templated Bilayer Films of Block Copolymers

Kevin W. Gotrik^{†1}, Thomas Lam^{†2}, Adam F. Hannon¹, Wubin Bai¹, A. Alexander-Katz¹, J. Alexander
Little², C. A. Ross^{1*}

¹ *Department of Materials Science and Engineering, Massachusetts Institute of Technology,
77 Massachusetts Avenue, Cambridge, Massachusetts 02139*

² *Center for Nanoscale Science and Technology, National Institute of Standards and Technology*

[†]*Authors contributed equally to this work*

^{*}*Address correspondence to caross@mit.edu*

Supplementary Information

1. Quantitative data from TEM Tomography

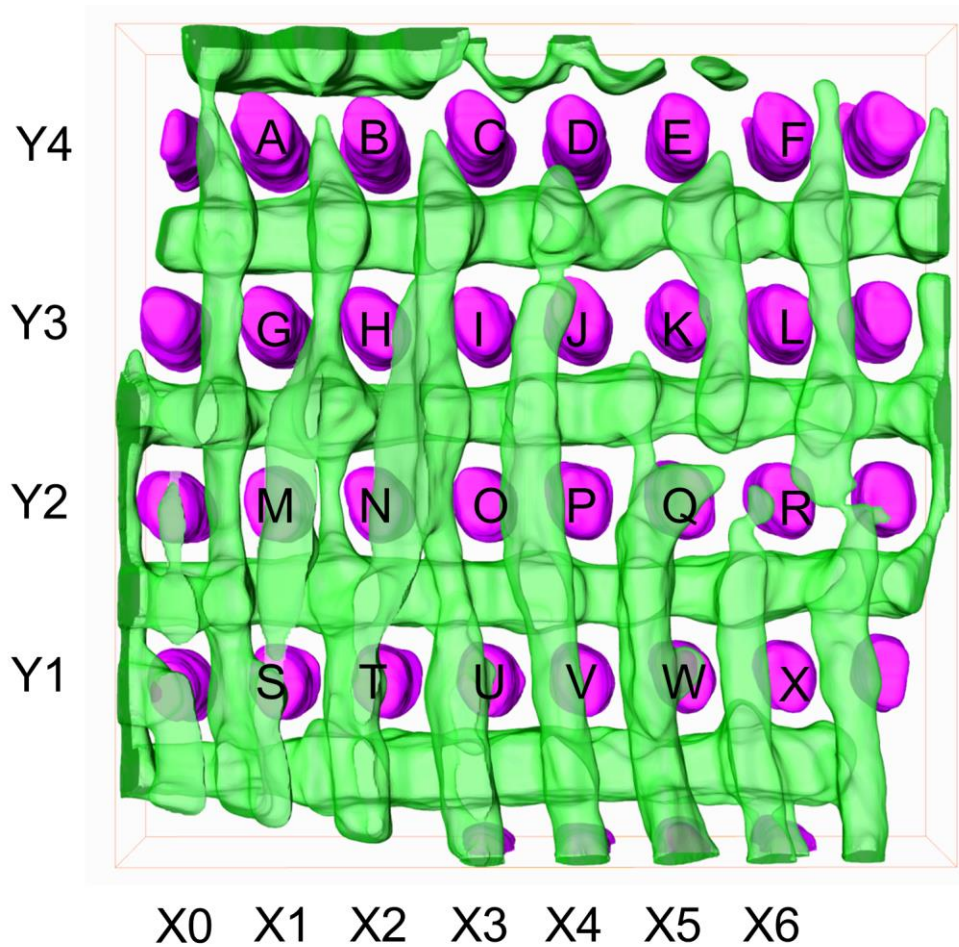


Figure S1. Unetched sample labelled to identify the posts. Their heights are given in Table S1.

Table SI. Quantitative Statistics on HSQ Posts

Post	Diameter (nm)	Circularity	Height (nm) *
A	21 ± 2	0.86 ± 0.04	29
B	20 ± 2	0.87 ± 0.03	29
C	20 ± 1	0.86 ± 0.03	27
D	20 ± 1	0.88 ± 0.03	26
E	20 ± 1	0.87 ± 0.02	22
F	20 ± 1	0.86 ± 0.03	23
G	20 ± 1	0.86 ± 0.08	23
H	20 ± 1	0.86 ± 0.04	23
I	20 ± 1	0.86 ± 0.04	23
J	21 ± 1	0.86 ± 0.03	23
K	20 ± 2	0.86 ± 0.04	22
L	20 ± 2	0.86 ± 0.04	21
M	21 ± 1	0.88 ± 0.03	22
N	20 ± 1	0.88 ± 0.03	21
O	20 ± 1	0.87 ± 0.03	20
P	20 ± 2	0.86 ± 0.03	20
Q	21 ± 2	0.83 ± 0.06	19
R	21 ± 1	0.86 ± 0.04	17
S	20 ± 1	0.88 ± 0.03	20
T	19 ± 2	0.86 ± 0.03	20
U	20 ± 1	0.87 ± 0.04	17
V	19 ± 2	0.86 ± 0.02	17
W	20 ± 1	0.86 ± 0.05	17
X	19 ± 1	0.86 ± 0.06	17
Average	20	0.86	
Standard Deviation	1	0.01	

*Standard Deviation of the measurements made for the HSQ post height was less than 1 nm.

Table SII. Post heights and SCFT Prediction

$\chi N = 30$							$\chi N = 24$						
SCFT, h_p/L_0	X1	X2	X3	X4	X5	X6	SCFT, h_p/L_0	X1	X2	X3	X4	X5	X6
Y4	h, 0.81	h, 0.81	h, 0.75	c, 0.72	c, 0.61	c, 0.64	Y4	i, 0.81	i, 0.81	i, 0.75	h, 0.72	b, 0.61	b, 0.64
Y3	c, 0.64	c, 0.64	c, 0.64	c, 0.64	c, 0.61	c, 0.58	Y3	b, 0.64	b, 0.64	b, 0.64	b, 0.64	b, 0.61	b, 0.58
Y2	c, 0.61	c, 0.58	c, 0.56	c, 0.56	c, 0.53	c, 0.47	Y2	b, 0.61	b, 0.58	b, 0.56	b, 0.56	c, 0.53	c, 0.47
Y1	c, 0.56	c, 0.56	c, 0.47	c, 0.47	c, 0.47	c, 0.47	Y1	b, 0.56	b, 0.56	c, 0.47	c, 0.47	c, 0.47	c, 0.47

In this Table, the predictions of SCFT are shown for each post height h_p , for two values of χN , and with neutral substrate and air surfaces and PS-preferential posts. The predicted morphology of the block copolymer is shown with a color and a letter (b, c, h or i) corresponding to Fig. 5 of the main text. The morphology h (dark blue) is the connected mesh structure which is predicted for the taller posts A-D for some values of χN . Experimentally, the connected mesh was observed throughout the sample.

Table SIII. Quantitative Statistics on PDMS from the Bottom Layer

PDMS cylinder below post row	Measured close to Post	PDMS Cylinder Height (nm)	Circularity
Y4	A	15 ± 1	0.73 ± 0.03
Y4	B	15*	0.77 ± 0.02
Y4	C	19 ± 2	0.77 ± 0.04
Y4	D	14 ± 2	0.74 ± 0.06
Y4	E	17 ± 4	0.74 ± 0.12
Y4	F	14 ± 2	0.68 ± 0.07
Y3	G	16 ± 2	0.83 ± 0.02
Y3	H	15 ± 1	0.84 ± 0.02
Y3	I	20 ± 2	0.81 ± 0.01
Y3	J	23*	0.79 ± 0.01
Y3	K	15 ± 1	0.74 ± 0.06
Y3	L	15 ± 1	0.78 ± 0.06
Y2	M	13 ± 1	0.77 ± 0.03
Y2	N	18*	0.84 ± 0.04
Y2	O	19*	0.84 ± 0.02
Y2	P	17 ± 2	0.81 ± 0.06
Y2	Q	13*	0.78 ± 0.02
Y2	R	23 ± 1	0.74 ± 0.03
Y1	S	11 ± 3	0.70 ± 0.06
Y1	T	19 ± 1	0.79 ± 0.03
Y1	U	18*	0.79 ± 0.03
Y1	V	14 ± 1	0.73 ± 0.02
Y1	W	13 ± 4	0.72 ± 0.02
Y1	X	17*	0.74 ± 0.03

*Standard Deviation of the measurements made in this PDMS region was less than 1 nm.

This Table gives the diameter (height) of the cylinders measured in the out-of-plane direction, for the bottom layer cylinders in various locations near the posts. All of the cylinders showed an elliptical cross-section with the in-plane diameter larger than the out-of-plane diameter.

Table SIV. Quantitative Statistics on PDMS from the Top Layer

PDMS cylinder to left of post column	Measured close to Post	PDMS Cylinder Height (nm)	Circularity
X1	A	9 ± 3	0.90 ± 0.06
X1	G	8 ± 1	0.92 ± 0.06
X1	M	7*	0.93 ± 0.03
X1	S	10 ± 1	0.92 ± 0.06
X2	B	7 ± 2	0.91 ± 0.08
X2	H	8 ± 2	0.89 ± 0.06
X2	N	4 ± 2	0.97 ± 0.04
X2	T	12 ± 1	0.89 ± 0.06
X3	C	8 ± 3	0.91 ± 0.07
X3	I	10 ± 1	0.85 ± 0.08
X3	O	9*	0.94 ± 0.01
X3	U	13 ± 1	0.85 ± 0.08
X4	D	4 ± 2	0.85 ± 0.14
X4	J	9 ± 1	0.81 ± 0.05
X4	P	11*	0.77 ± 0.03
X4	V	10*	0.81 ± 0.05
X5	E	7 ± 3	0.87 ± 0.11
X5	K	10 ± 3	0.78 ± 0.06
X5	Q	13 ± 1	0.70 ± 0.10
X5	W	12 ± 1	0.78 ± 0.06
X6	F	6 ± 2	0.92 ± 0.07
X6	L	8 ± 1	0.86 ± 0.05
X6	R	11 ± 1	0.46 ± 0.04
X6	X	8 ± 1	0.86 ± 0.05

*Standard Deviation of the measurements made in this PDMS region was less than 1 nm.

Note: PDMS regions left of posts E and K contain very few measurements; the non-constraint smoothing applied in the 3D visualization is why the measurements are not seen in the tomography image of Fig. S1.

This Table gives the diameter (height) of the cylinders measured in the out-of-plane direction, for the top layer cylinders, in various locations near the posts. All of the cylinders showed an elliptical cross-section with the in-plane diameter larger than the out-of-plane diameter. However, they are less elliptical than the bottom layer cylinders.

2. Details of the SCFT Modeling

BCP systems have been modeled using SCFT simulations in terms of predicting phase behavior as a function of control variables. SCFT allows the computational prediction of the equilibrium morphological behavior of BCPs under a variety of boundary conditions and with the incorporation of a variety of other components such as homopolymers, solvents, or other BCPs [ref. S1-S5].

In SCFT, one starts with the partition function Z which is a functional of a Hamiltonian H that represents the free energy of the system when evaluated at a field solution. Instead of writing H as an explicit function of monomer positions along the chain, it is written in terms of chemical potential fields Ω and density fields ρ . These fields are functions of spatial coordinates $\vec{\mathbf{r}} = \{\mathbf{x}, \mathbf{y}, \mathbf{z}\}$. Z is given mathematically as

$$Z = \int e^{\frac{-H[\rho, \Omega]}{kT}} D\rho D\Omega$$

where k is the Boltzmann constant, T is the temperature, D represents integration over a function, and the spatial dependence of ρ and Ω have been suppressed for clarity. The condition that is then sought in SCFT simulations is the set of $\rho = \rho^*$ and $\Omega = \Omega^*$ that satisfy the mean-field saddle point equations

$$\left. \frac{\delta H}{\delta \rho} \right|_{\rho^*} = 0 \text{ and } \left. \frac{\delta H}{\delta \Omega} \right|_{\Omega^*} = 0$$

which in the polymer community are referred to as the SCFT conditions since they satisfy the self-consistent equations of the mean-field theory. Once found, ρ^* and Ω^* represent the morphology of an equilibrium structure the BCP forms under the specified boundary conditions and control parameter values given in the simulation. Since these are general saddle point equations, the structure found may not be a global energy minimum, thus multiple simulations are generally necessary to ensure the structure found is indeed the global minimum energy solution and not a local solution. However, such local solutions are of interest since experimental systems can get trapped in such states as well depending on how the system is annealed.

By using a continuous Gaussian chain model and assuming the system is a diBCP, the density field equation component of the partition function can be integrated out and the problem collapses to a problem of just finding two independent chemical potential fields. For the diBCP system considered in this study, H is given as

$$H[\Omega_+, \Omega_-] = c \left(\int d\vec{\mathbf{r}} \left((2f - 1) \Omega_- + \frac{\Omega_-^2}{\chi N} - \Omega_+ \right) - V \ln(Q[\Omega_+, \Omega_-]) \right)$$

where f is the volume fraction of the minority component (PDMS in the system studied), χ is the Flory-Huggins interaction parameter that measures the enthalpic difference in the blocks (higher χ means the polymers are harder to mix), N is the degree of polymerization (number of chemical monomers in the chain), V is the volume of the simulation unit cell, Ω_+ is the pressure-like chemical potential field, Ω_- is the exchange interaction chemical potential field, and C is a constant without dimensions representing the concentration of the monomers in the polymer chain such that $C = \frac{\rho_0 R_g^3}{N}$ with ρ_0 being the density of monomer in the chain and R_g being the radius of gyration of the polymer. Q here is the single chain partition function under the mean field conditions and is found by solving for the propagators q such that

$$Q[\boldsymbol{\mu}] = \frac{1}{V} \int d\vec{r} q(\vec{r}, s = 1, \boldsymbol{\mu})$$

where q propagators are found using the Fokker-Plank diffusion equations

$$\frac{\partial q(\vec{r}, s, \boldsymbol{\mu})}{\partial s} = \frac{R_g^2}{N} \nabla^2 q(\vec{r}, s, \boldsymbol{\mu}) - \boldsymbol{\mu}(\boldsymbol{\phi}(\vec{r}, s, \boldsymbol{\mu})) q(\vec{r}, s, \boldsymbol{\mu})$$

with initial conditions

$$q(\vec{r}, 0, \boldsymbol{\mu}) = 1$$

where s is the measured position along the chain such that $s = 0$ is the start of the chain from the minority (PDMS) end and $s = 1$ is the chain end at the PS side, $\boldsymbol{\mu}$ is the chemical potential field corresponding to either the PDMS or PS chain such that

$$\boldsymbol{\mu} = \begin{cases} \Omega_{PDMS} = \Omega_+ + \Omega_- & s < f \\ \Omega_{PS} = \Omega_+ - \Omega_- & s \geq f \end{cases}$$

and $\boldsymbol{\phi}$ represents the normalized densities found as follows

$$\boldsymbol{\phi}(\vec{r}) = \begin{cases} \phi_{PDMS}(\vec{r}) = \frac{\rho(\vec{r})}{\rho_0} = \frac{1}{Q} \int_0^f ds q^\dagger(\vec{r}, 1 - s, \boldsymbol{\mu}) q(\vec{r}, s, \boldsymbol{\mu}) \\ \phi_{PS}(\vec{r}) = \frac{\rho(\vec{r})}{\rho_0} = \frac{1}{Q} \int_f^1 ds q^\dagger(\vec{r}, 1 - s, \boldsymbol{\mu}) q(\vec{r}, s, \boldsymbol{\mu}) \end{cases}$$

where q^\dagger is the propagator found solving the Fokker-Planck diffusion equation starting at the $s = 1$ (PS) end of the chain. The Fokker-Planck equations can be solved in a variety of ways. For the system studied, a pseudo-spectral method was chosen [ref. S2].

For initializing the system, random values are assigned to the Ω_- field and the system is solved iteratively using a steepest descent complex Langevin relaxation scheme. Since the condition that is sought to be satisfied is $\left. \frac{\delta H}{\delta \Omega} \right|_{\Omega^*} = 0$, the field time evolution in the simulation across iterations is set equal to the Hamiltonian field derivatives with a proportionality constant as follows

$$\frac{\delta \Omega_+}{dt} = \lambda_+ \frac{\delta H}{\delta \Omega_+} \text{ and } \frac{\delta \Omega_-}{dt} = \lambda_- \frac{\delta H}{\delta \Omega_-}$$

where λ_+ and λ_- are set larger enough to make the system converge in as few iterations as possible but small enough the system does not become numerically unstable. t here is a time step in terms of forward iteration number in the simulation. For the system studied, the time constants were optimized to values $\lambda_+ = 5.0$ and $\lambda_- = 0.0033$ through computational trial and error. Using the Hamiltonian H , these derivatives are found to be

$$\frac{\delta\Omega_+}{dt} = \lambda_+ C(1 - \phi_+) \text{ and } \frac{\delta\Omega_-}{dt} = -\lambda_- C \left(2f - 1 - \phi_- - \frac{2\Omega_-}{\chi N} \right)$$

and converting the equations to be numerically implementable

$$\begin{aligned} \Omega_{+,j+1} &= \Omega_{+,j} + \lambda_+ C(1 - \phi_{+,j}) \\ \Omega_{-,j+1} &= \Omega_{-,j} - \lambda_- C \left(2f - 1 - \phi_{-,j} - \frac{2\Omega_{-,j}}{\chi N} \right) + \lambda_- \eta(\vec{r}) \end{aligned}$$

where j represents the j th iteration. Notice the term $\eta(\vec{r})$ was added to the second update scheme equation for Ω_- . This is a Gaussian random noise term used in complex Langevin dynamics schemes that helps to keep the system out of very shallow metastable solutions.

Calculations were performed on a discrete grid of N_x by N_y by N_z grid points representing the real 3D spatial locations of a periodically bound system with posts. $N_x = 24$ and $N_y = 14$ for all simulations while N_z was either 28, 36, or 42 for $2.0 L_0$, $2.5 L_0$, or $3.0 L_0$ thick films respectively. Matrices representing the field variables were used in these calculations. The boundary conditions of the system are schematically shown in Fig. S2. These boundary conditions correspond to constraining the fields in different regions to have fixed values such that in the post regions no polymer density evolves and in the brush layer and air interface regions a certain surface affinity is fixed. In terms of the field parameters, these constraints amount to the following:

$$\Omega_+ = P = 20 \text{ if grid point is in a post or the substrate.}$$

$$\Omega_- = W_{Air} \text{ if grid point is in the air interface region.}$$

$$\Omega_- = W_{PBL} \text{ if grid point is in the post brush layer region.}$$

$$\Omega_- = W_{SBL} \text{ if grid point is in the substrate brush layer region.}$$

The values of W were 0 if neutral, -10 if preferential to PDMS, and 10 if preferential to PS. These field constraint values were established in previous studies based on the maximum field values inside the self-consistent solutions for hexagonal post array templated PS-PDMS [ref. S5-S6].

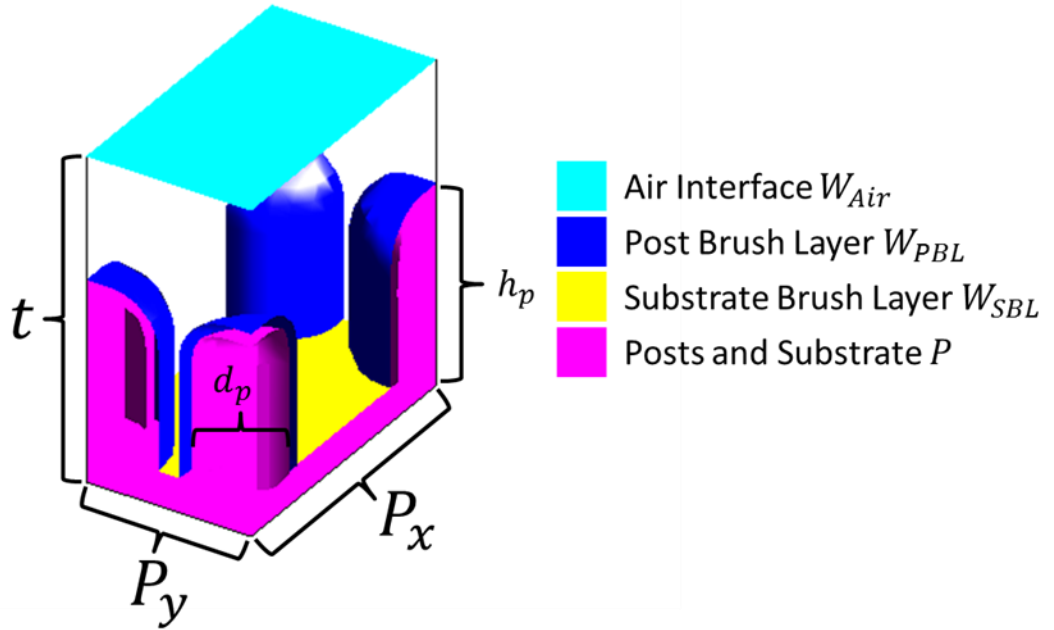


Figure S2. Schematic of boundary conditions used in SCFT simulations. Cyan region was modeled as either a PDMS preferential $W_{Air} = -10$ or neutral air interface $W_{Air} = 0$. Blue region was modeled as preferential to PS $W_{PBL} = 10$ to represent the PS brush. Yellow region was modeled as either PS preferential $W_{SBL} = 10$ or neutral substrate brush layer $W_{SBL} = 0$. Purple regions were modeled as hard wall boundary conditions for posts and the substrate $P = 20$. t , the film thickness, was varied between $2.0 L_0$, $2.5 L_0$, and $3.0 L_0$. P_y , the post period in the y –direction, was set equal to L_0 , P_x , the post period in the x –direction, was set equal to $1.71 L_0$, and d_p , the post diameter, was set equal to $0.71 L_0$. h_p , the post height, was varied depending on the film thickness over a larger range of heights. L_0 was taken to be 36 nm for SCFT calibration with real measured distances.

SCFT simulations were performed over a range of parameters to gauge which simulation parameters best corresponded to the experimental 3D TEM tomography data. Due to uncertainty in the substrate affinity (i.e. how preferential the silicon nitride functionalized with a PS-brush layer is to the PS block) and how preferential the top surface is to PDMS during the solvent annealing, different surface conditions were explored in the simulations. These conditions influence the commensurate thickness at which different numbers of layers of block copolymer microdomains form. In all cases explored, the posts were assumed to still be PS preferential due to the experimental observation that the minority PDMS avoids contact with the posts in almost all locations on the substrate.

For neutral top and bottom surface affinity conditions, two layers of microdomains are commensurate at a film thickness of $2.0 L_0$. For a PDMS-preferential top surface and a neutral bottom surface, two layers of features are commensurate at a thickness of $2.5 L_0$. For a PDMS-preferential top surface and PS-preferential bottom surface, two layers of features are

commensurate at a thickness of $3.0 L_0$. Due to the different thickness requirements for different surface affinity conditions, the range of post heights explored in the model was changed. Thus the post heights explored for the $2.0 L_0$ and $2.5 L_0$ -thick films were from $0.07 L_0$ to $1.43 L_0$ in steps of $0.07 L_0$. The post heights explored in the $3.0 L_0$ case were from $0.14 L_0$ to $2.86 L_0$ in steps of $0.14 L_0$.

Comparing the 3D TEM tomography results with the SCFT results is based on the following considerations. The unetched samples are collapsed from their swollen equilibrium structure, and their dimensions in the out-of-plane direction were scaled by the swelling factor for direct comparison with the SCFT results. The observed TEM results showed a collapsed film thickness of ≈ 40 nm and the swelling ratio was around 2.3. This gives a swollen film thickness of ~ 90 nm. L_0 for this system is ≈ 36 nm, thus these swollen film thickness correspond roughly to $2.5 L_0$. The height of the posts where the mesh structure with connections was observed experimentally was ≈ 34 nm, or $\approx 0.9L_0$. The mesh structure is predicted for these post heights in simulations with neutral bottom and top surfaces, or to a lesser extent for simulations with neutral bottom and PDMS-preferential top surfaces, but not for simulations with PS-preferential bottom surface and PDMS-preferential top surface. The actual experimental conditions likely have some PS wetting of the bottom surface and a neutral top surface due to the solvent annealing conditions of 5:1 toluene to heptane. Evidence for the surface chemistry is presented later in the SI.

In our previous study of the mesh structure [ref. S6], the modeling was limited to $\chi N = 30$ and $f = 0.32$ with the top surface PDMS preferential and the bottom PS preferential, and $h_p = 1.71 L_0$. In that study the bottom surface was likely more preferential to PS as the substrate was SiO_2 instead of nitride.

Choosing the simulations that best match the experimental conditions along with morphology, we compared the dimensions from the unetched 3D TEM tomography data with the simulation data. For neutral top and bottom surface conditions, a post height of $0.93 L_0$, $\chi N = 30$, and $f = 0.36$ gave the interconnected mesh that matched the experimental results the best. Comparisons of two cross-sections of the simulation results with the experiment are shown in the main text in Fig. 6. These measurements were made by counting the number of grid points between $\phi = 0.5$ surface layers for the PDMS in the simulation and multiplying that count by the minimum resolution of 2.57 nm. Additional simulation images and cross-section measurements are shown below in Fig. S3 through Fig. S8.

The resolution of the SCFT simulations is 2.57 nm based on the coarse-graining of the simulation such that one grid point corresponds to $\frac{L_0}{14} \approx \frac{36 \text{ nm}}{14} = 2.57$ nm. This is obtained using the fact that 14 grid points represented a length of L_0 in the simulations. The post pitch dimensions were 36 nm by 62 nm (14 by 24 grid points) in the simulations to best match the nominal dimensions written by the electron beam lithography tool, although the actual measured

dimensions differed slightly (≈ 34 nm by ≈ 65 nm), possibly due to drift or calibration errors during writing.

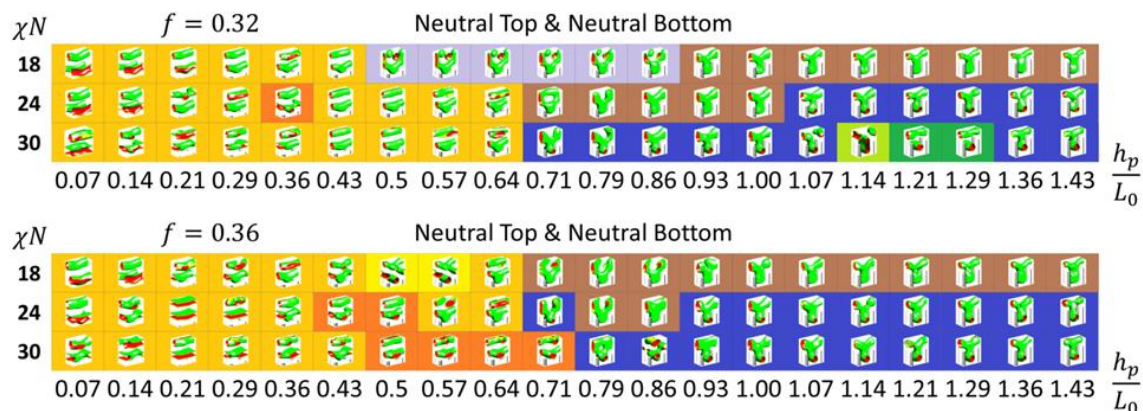


Figure S3. SCFT simulation results for neutral top and bottom surface conditions. This data augments Fig. 5 by showing the calculated morphology as an inset within each colored square. The colors match those of Fig. 5.

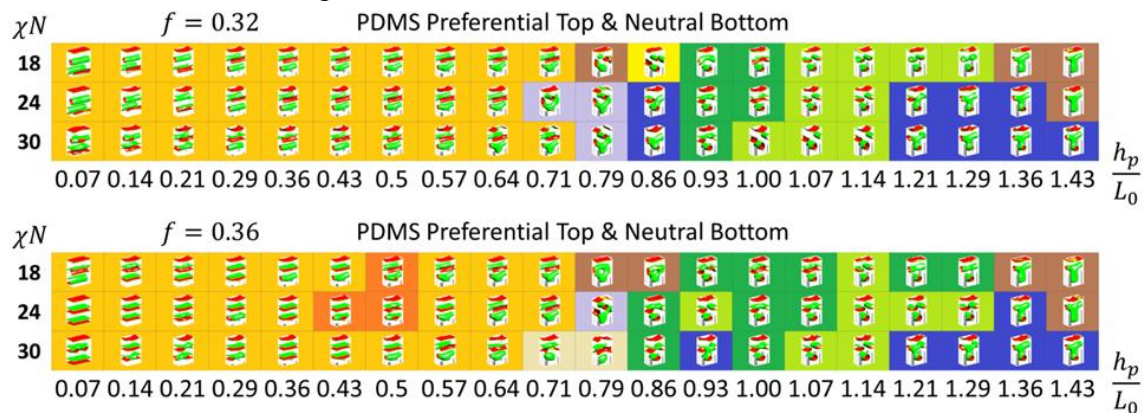


Figure S4. SCFT simulation results for PDMS preferential top and neutral bottom surface conditions.

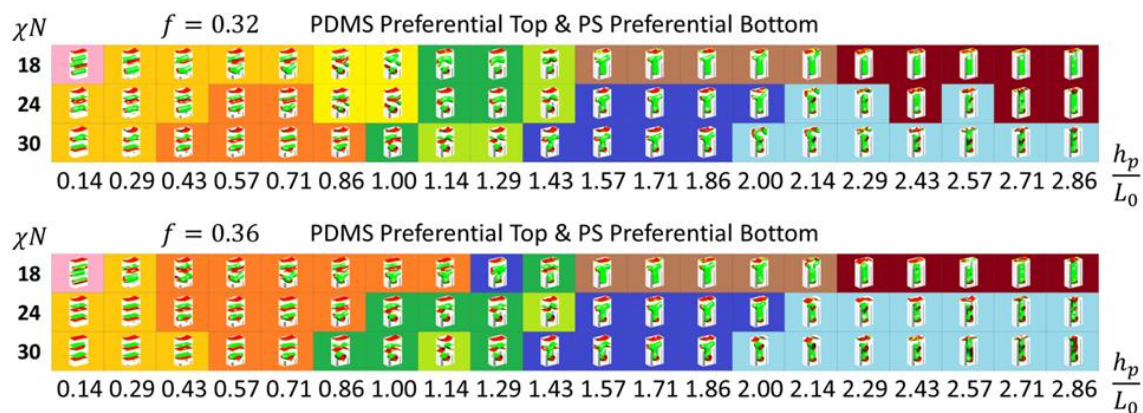


Figure S5. SCFT simulation results for PDMS preferential top and PS preferential bottom surface conditions.

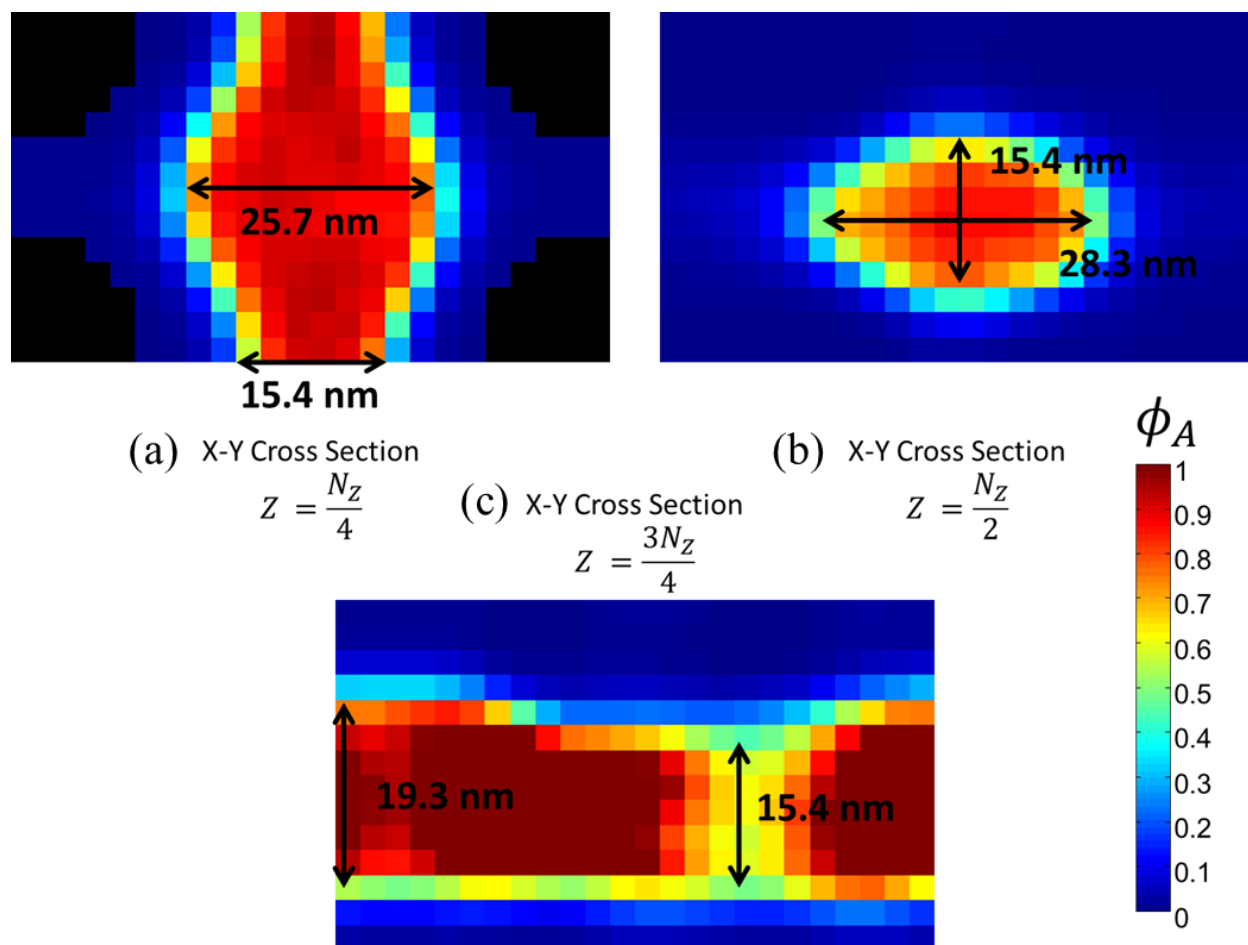
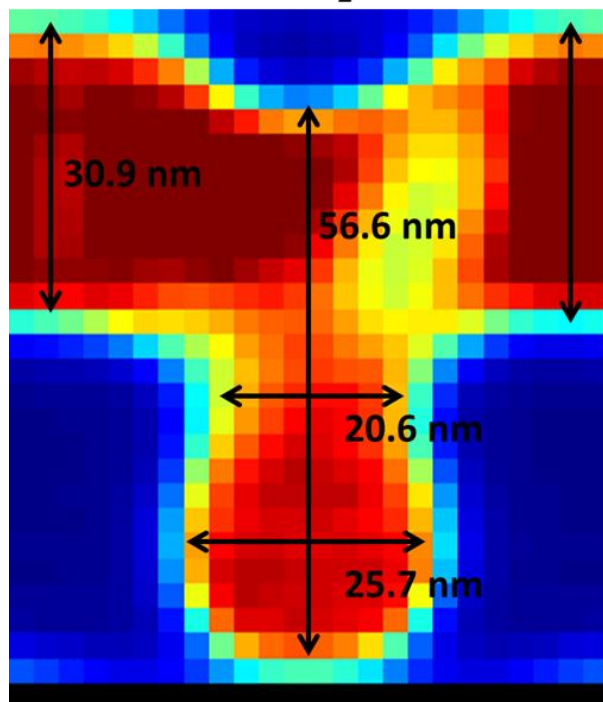


Figure S6. SCFT simulation cross-section results in the X-Y plane at different heights for the best matching mesh structure simulation at a post height of $0.93 L_0$, $\chi N = 30$, and $f = 0.36$. The cross-sections (a), (b), and (c) correspond to sections through the bottom cylinder $Z = N_Z/4$, through the junction $Z = N_Z/2$, and through the top cylinder $Z = 3N_Z/4$ respectively.

(a) X-Z Cross Section
 $Y = \frac{N_Y}{2}$



(b) X-Z Cross Section
 $Y = N_Y$

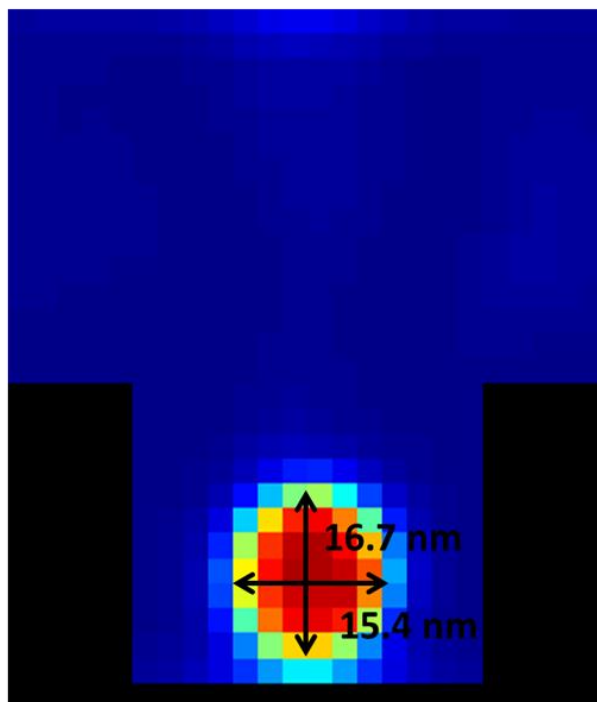
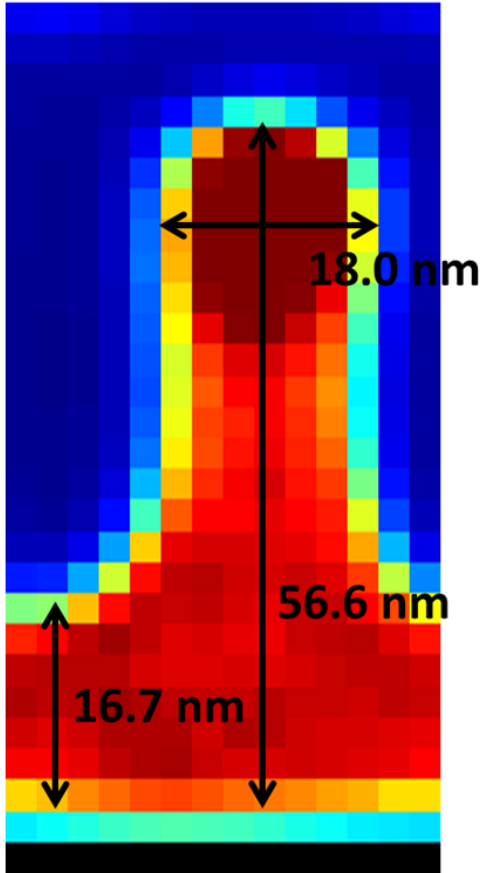


Figure S7. SCFT simulation cross-section results in the X-Z plane for the best matching mesh structure simulation at a post height of $0.93L_0$, $\chi N = 30$, and $f = 0.36$. (a) is half way between posts at $Y = N_Y/2$. (b) is through the line of posts at $Y = N_Y$.

(a) Y-Z Cross Section

$$X = \frac{N_X}{2}$$



(b) Y-Z Cross Section

$$X = N_X$$

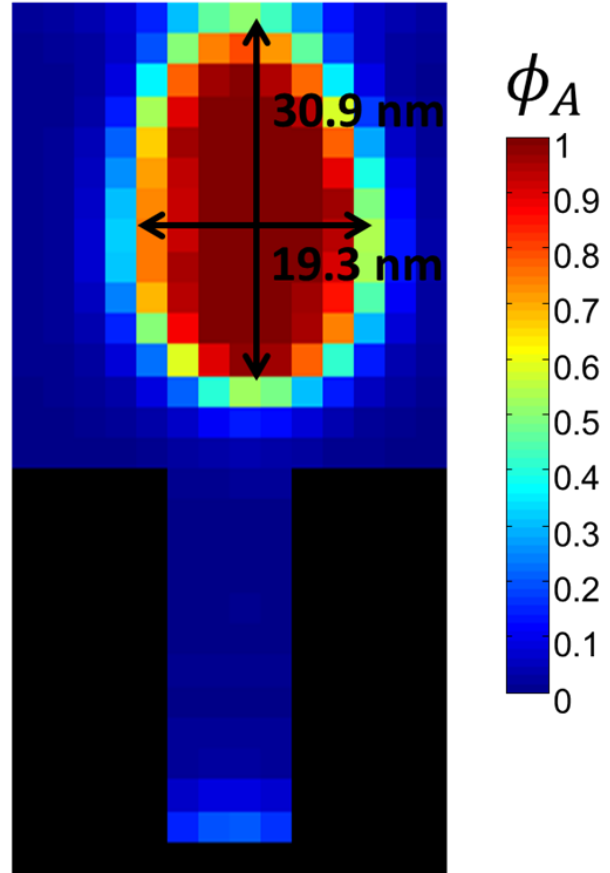


Figure S8. SCFT simulation cross-section results in the Y-Z plane for the best matching mesh structure simulation at a post height of $0.93L_0$, $\chi N = 30$, and $f = 0.36$. (a) is half way between posts at $X = N_X/2$. (b) is through the line of posts at $X = N_X$.

Table SV. Quantitative Measurements of SCFT Cylinder Dimensions

	Min. Diameter	Max. Diameter	Z-Dimension	Min. Error
Bottom Cylinder	15.4 nm	25.7 nm	16.7 nm	2.5 nm
Connection	15.4 nm	28.3 nm	20.6 nm	2.5 nm
Top Cylinder	15.4 nm	19.3 nm	30.9 nm	2.5 nm

This Table gives the measured dimensions of the different cylindrical features in the mesh structure for the best simulation result. Error is defined by the minimum grid point size.

3. Tomography data for posts before RIE

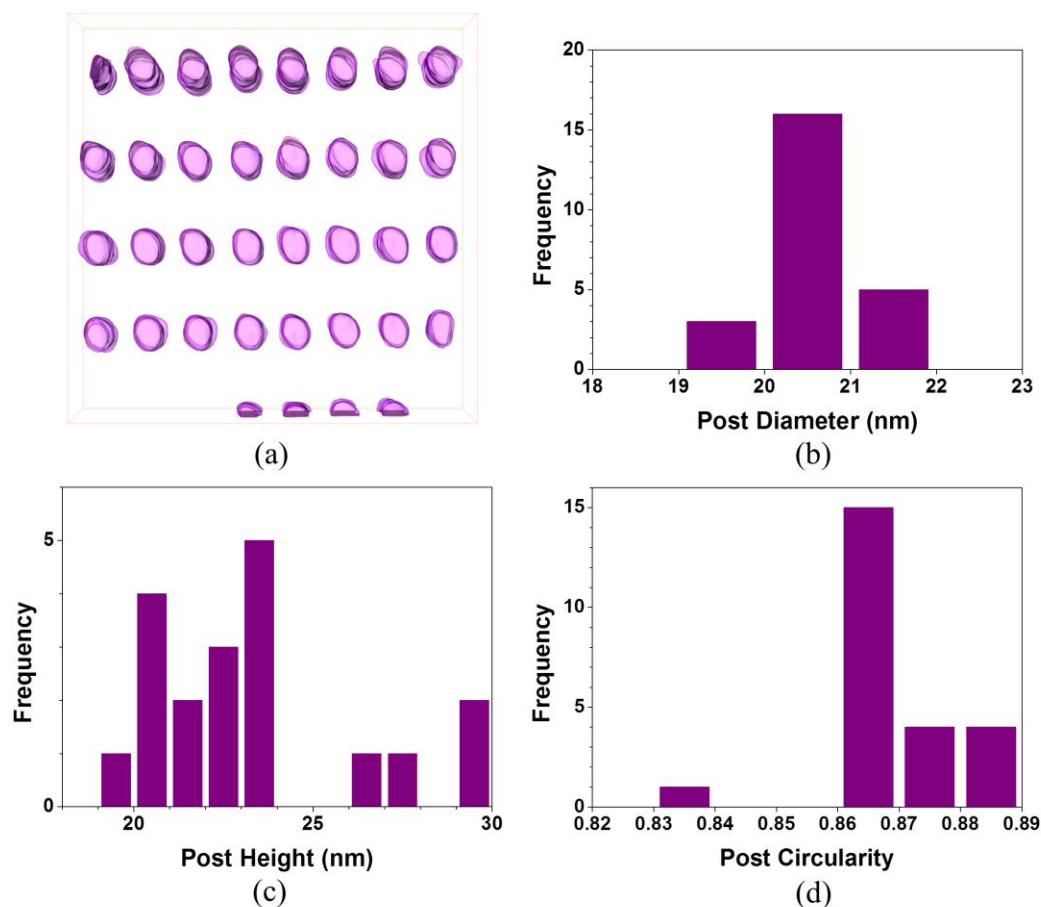


Figure S9. (a) Experimental TEM tomography image of just the HSQ posts before reactive ion etching; (b) histogram of post diameter before reactive ion etching; (c) histogram of post height before reactive ion etching; (d) histogram of post circularity before reactive ion etching.

The dimensions of the posts as well as their surface energy was found to have an important influence on the alignment and registration of the self-assembled cylinders. Fig. S9 shows the uniformity of the templated HSQ posts from the TEM tomography. The post diameter and circularity had excellent uniformity while a slightly non-uniform post height was observed. The non-uniformity of post height was presumed due to the difficulty of uniform HSQ spin-casting over the small sample. Comparing the contour plot of HSQ post heights (Fig. 3(a)) with the 3D visualization of the self-assembled structure (Fig. 4(b)), in the region where HSQ posts heights were relatively low ($h_p/L_0 = 0.54$), the PDMS cylinders tended to cover part of the posts while in the region with higher posts ($h_p/L_0 = 0.63$), double layers of PDMS cylinders were well aligned in the interconnected mesh.

4. Chemistry of the air interface and substrate

a) Top surface of film

The difference in surface energy γ between PS ($\gamma_{\text{PS}} \approx 40.7$ mN/m) and PDMS ($\gamma_{\text{PDMS}} \approx 20.4$ mN/m) [ref. S7] promotes the formation of a layer of PDMS at the air interface. This is seen from etching studies, where the PDMS surface layer has first to be removed by a short CF_4 etch before the PS can be etched by oxygen. Fig. S10 shows the difference between morphologies with and without a 5 s CF_4 plasma etching step preceding O_2 plasma etching. The morphology looks similar in both cases, which suggests that there was little or no PDMS surface layer formed by the solvothermal anneal used here, consistent with the TEM observations. In (b), only small particles of oxidized PDMS were observed on the surface. The 5 min solvent flow annealing in toluene: heptane 5:1 with 30 s thermal quench appears to have minimized the formation of a PDMS surface layer, unlike what is seen in thermal annealing.

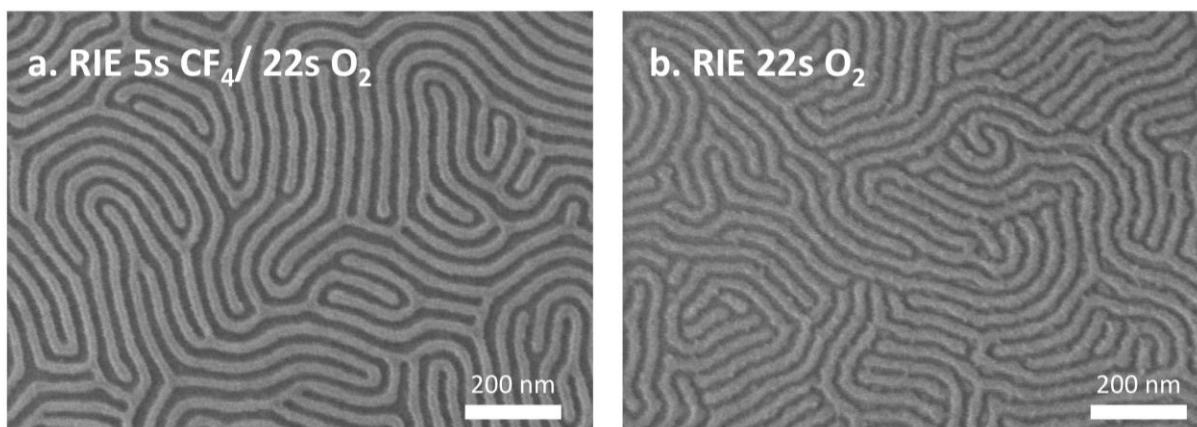


Figure S10. SEM images of self-assembled PS-*b*-PDMS block copolymer after (a) 5 s CF_4 and then 22s O_2 reactive ion etching treatment; (b) only 22s O_2 reactive ion etching treatment.

b) Characterization of the grafted polystyrene layer on the silicon nitride grid

X-ray photoelectron spectroscopy (XPS) was used to determine the adhesion of hydroxyl-terminated polystyrene brushes to a silicon nitride grid. A PHI Versaprobe II XPS was used with spot size of 10 μm , 1.25W, 5kV, spot analyzer pass energy of 117.4 eV, step size of 0.25 eV, and take-off angle 45° . Fig. S11 shows the spectra obtained from the surface of the silicon nitride grid with PS brush treatment. The strong carbon signal shows the existence of carbon on the silicon nitride grid and therefore indicates that the PS brush has been attached to the silicon nitride grid, at least to some extent. The nature of this attachment, either physical or chemical, and the grafting density is out of the scope of this study. Similar block copolymer morphologies were formed on a PS-coated nitride grid and a PS-coated nitride layer on a Si wafer indicating that grafting onto the membrane was the same as grafting onto a supported nitride layer.

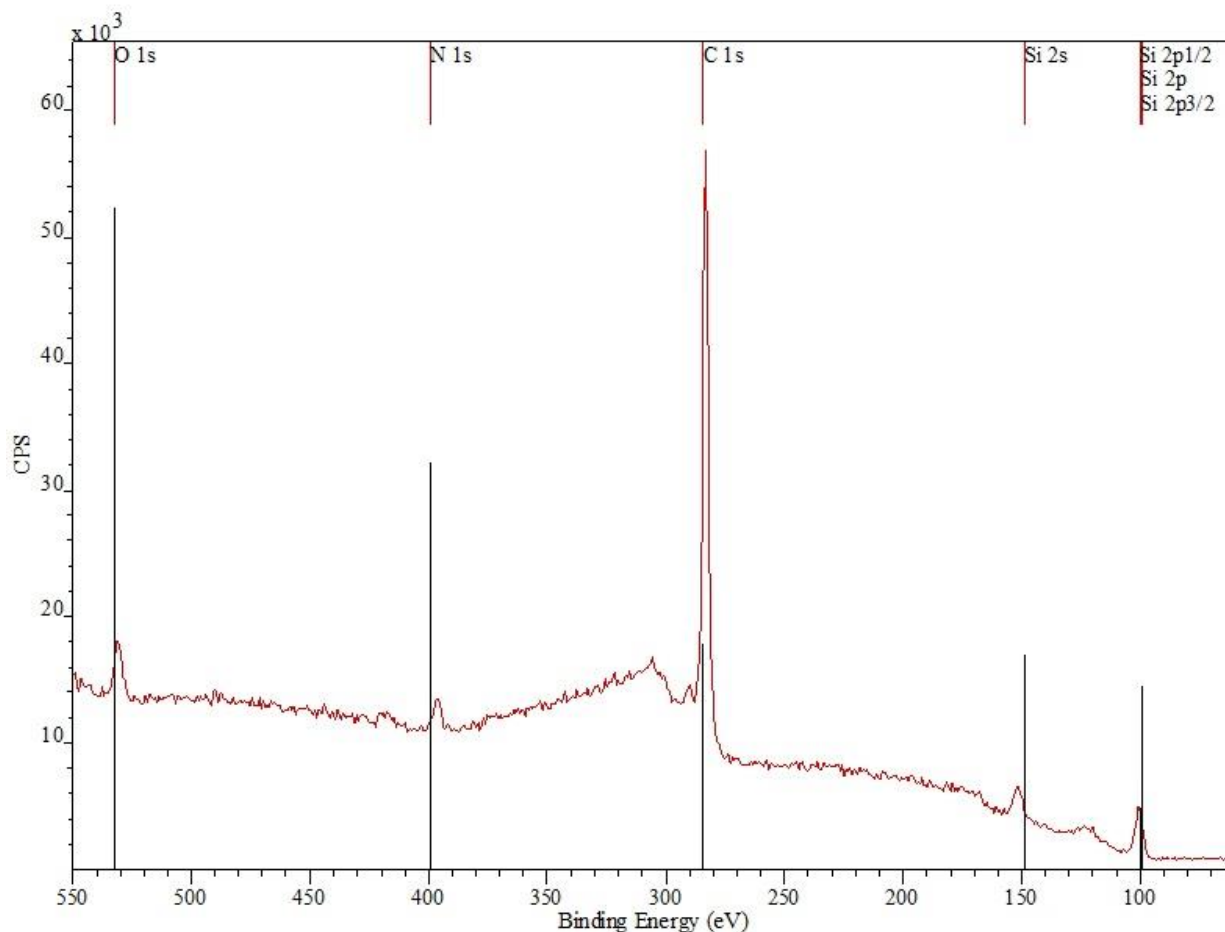


Figure S11. XPS analysis of surface chemistry of silicon oxide grid functionalized with polystyrene brush.

c) Etch rate of silicon nitride

An oxygen plasma has excellent etching selectivity between PS and PDMS and clearly reveals the PDMS microdomains. However, when the PS block had been fully removed, the oxygen plasma can interact with the silicon nitride substrate that supports the BCP film. This could lead to undercutting of the pillars or the bottom layer of PDMS microdomains. Therefore it is crucial to measure the oxygen etch rate of the silicon nitride substrate. Fig. S12 shows a linear relation between nitride thickness and the etching time for a nitrated Si wafer. For 22s oxygen RIE, which was the maximum that the nitride layer could have been exposed to during the etching of the TEM sample, only 0.4 nm thickness of nitride film was removed, therefore the effect of the oxygen plasma on silicon nitride support film can be neglected.

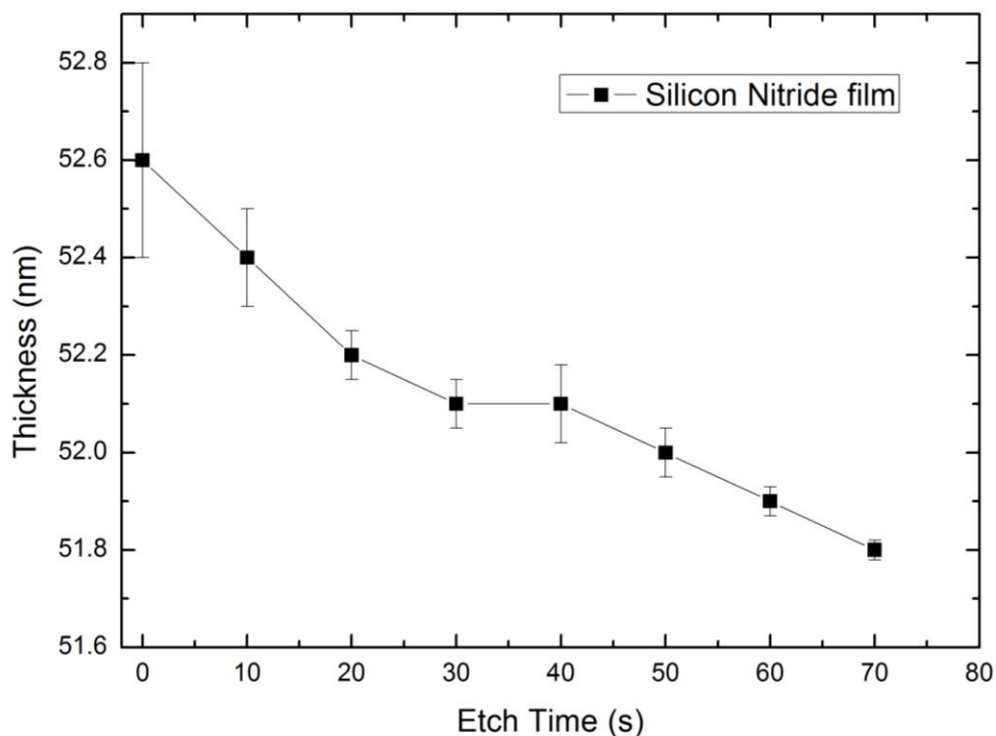


Figure S12. Etching rate of Silicon Nitride film under oxygen RIE with power 90 W and pressure 6 mTorr. The error bars of this graph are \pm one standard deviation of the average.

Ref. S1. Matsen, M.; Schick, M. Stable and Unstable Phases of a Diblock Copolymer Melt. *Physical Review Letters* **1994**, *72*, 2660–2663.

Ref. S2. Fredrickson, G. H. *The Equilibrium Theory of Inhomogeneous Polymers*; Oxford University Press: Oxford, England, **2006**.

Ref. S3. Fredrickson, G. H.; Ganesan, V.; Drolet, F. Field-Theoretic Computer Simulation Methods for Polymers and Complex Fluids. *Macromolecules* **2002**, *35*, 16–39.

Ref. S4. Alexander-Katz, A.; Fredrickson, G. H. Diblock Copolymer Thin Films: A Field-Theoretic Simulation Study. *Macromolecules* **2007**, *40*, 4075–4087.

Ref. S5. Mickiewicz, R. A.; Yang, J. K. W.; Hannon, A. F.; Jung, Y.; Alexander-katz, A.; Berggren, K. K.; Ross, C. A. Enhancing the Potential of Block Copolymer Lithography with Polymer Self-Consistent Field Theory Simulations. *Macromolecules* **2010**, *43*, 8290–8295.

Ref. S6. Tavakkoli K. G., A.; Gotrik, K. W. W.; Hannon, A. F. F.; Alexander-Katz, A.; Ross, C. A. A.; Berggren, K. K. K. Templating Three-dimensional Self-assembled Structures in Bilayer Block Copolymer Films. *Science* **2012**, *336*, 1294–1298.

Ref. S7. Wu, S. In *Polymer Handbook*; Brandrup, J., Immergut, E. H., Grulke, E. A., Abe, A., Bloch, D. R., Eds.; John Wiley & Sons: New York, **2005**; pp 521–541.